

MAJOR REPORT • **OPEN ACCESS**

# The solenoidal large intensity device (SoLID) for JLab 12 GeV

To cite this article: J Arrington *et al* 2023 *J. Phys. G: Nucl. Part. Phys.* **50** 110501







View the [article online](#) for updates and enhancements.

## You may also like

- [A proposed U.S./China theoretical/experimental collaborative effort on baryon resonance extraction](#)  
Pire N Working Group
- [Instrumentation and control selection for the 12 GeV Hall B magnets at Jefferson Lab](#)  
Probir K Ghoshal, Ramakrishna Bachimanchi, Ruben J Fair et al.
- [A MRPC prototype for SOLID-TOF in JLab](#)  
Y Wang, X Fan, J Wang et al.

## Major Report

# The solenoidal large intensity device (SoLID) for JLab 12 GeV

J Arrington<sup>1</sup> , J Benesch<sup>2</sup>, A Camsonne<sup>2</sup>, J Caylor<sup>3</sup>,  
J-P Chen<sup>2</sup>, S Covrig Dusa<sup>2</sup>, A Emmert<sup>4</sup>, G Evans<sup>5</sup> , H Gao<sup>6</sup>,  
J-O Hansen<sup>2</sup> , G M Huber<sup>7</sup> , S Joosten<sup>8</sup>, V Khachatryan<sup>6</sup>,  
N Liyanage<sup>4</sup>, Z-E Meziani<sup>8,\*</sup> , M Nycz<sup>4</sup>, C Peng<sup>8</sup>, M Paolone<sup>9</sup>,  
W Seay<sup>2</sup>, P A Souder<sup>3</sup>, N Sparveris<sup>10</sup>, H Spiesberger<sup>11</sup>,  
Y Tian<sup>3</sup>, E Voutier<sup>12</sup>, J Xie<sup>8</sup>, W Xiong<sup>13</sup> , Z-Y Ye<sup>14</sup>, Z Ye<sup>15</sup>,  
J Zhang<sup>4</sup>, Z-W Zhao<sup>6</sup> and X Zheng<sup>4</sup> and  
For the Jefferson Lab SoLID Collaboration

<sup>1</sup> Lawrence Berkeley National Laboratory, Berkeley, CA, United States of America

<sup>2</sup> Thomas Jefferson National Accelerator Facility, Newport News, VA, United States of America

<sup>3</sup> Syracuse University, Syracuse, NY, United States of America

<sup>4</sup> University of Virginia, Charlottesville, VA, United States of America

<sup>5</sup> Brigham Young University—Idaho Rexburg, ID, United States of America

<sup>6</sup> Duke University and Triangle Universities Nuclear Laboratory, Durham, NC, United States of America

<sup>7</sup> University of Regina, Regina, SK, Canada

<sup>8</sup> Argonne National Laboratory, Argonne, IL, United States of America

<sup>9</sup> New Mexico State University, Las Cruces, NM, United States of America

<sup>10</sup> Temple University, Philadelphia, PA, United States of America

<sup>11</sup> PRISMA+ Cluster of Excellence, Institut für Physik, Johannes Gutenberg Universität, D-55099 Mainz, Germany

<sup>12</sup> Université Paris-Saclay, CNRS/IN2P3, IJCLab, Orsay, France

<sup>13</sup> Shandong University, Qingdao, People's Republic of China

<sup>14</sup> University of Illinois at Chicago, Chicago, IL, United States of America

<sup>15</sup> Tsinghua University, Beijing, People's Republic of China

E-mail: [jpchen@jlab.org](mailto:jpchen@jlab.org), [gao@phy.duke.edu](mailto:gao@phy.duke.edu), [zmeziani@anl.gov](mailto:zmeziani@anl.gov), [souder@phy.syr.edu](mailto:souder@phy.syr.edu) and [xiaochao@jlab.org](mailto:xiaochao@jlab.org)

Received 11 April 2023

Accepted for publication 31 May 2023

Published 25 September 2023



CrossMark

\* Author to whom correspondence should be addressed.



Original content from this work may be used under the terms of the [Creative Commons Attribution 4.0 licence](https://creativecommons.org/licenses/by/4.0/). Any further distribution of this work must maintain attribution to the author(s) and the title of the work, journal citation and DOI.

**Abstract**

The solenoidal large intensity device (SoLID) is a new experimental apparatus planned for Hall A at the Thomas Jefferson National Accelerator Facility (JLab). SoLID will combine large angular and momentum acceptance with the capability to handle very high data rates at high luminosity. With a slate of approved high-impact physics experiments, SoLID will push JLab to a new limit at the QCD intensity frontier that will exploit the full potential of its 12 GeV electron beam. In this paper, we present an overview of the rich physics program that can be realized with SoLID, which encompasses the tomography of the nucleon in 3D momentum space from semi-inclusive deep inelastic scattering, expanding the phase space in the search for new physics and novel hadronic effects in parity-violating DIS, a precision measurement of  $J/\psi$  production at threshold that probes the gluon field and its contribution to the proton mass, tomography of the nucleon in combined coordinate and momentum space with deep exclusive reactions, and more. To meet the challenging requirements, the design of SoLID described here takes full advantage of recent progress in detector, data acquisition and computing technologies. In addition, we outline potential experiments beyond the currently approved program and discuss the physics that could be explored should upgrades of CEBAF become a reality in the future.

**Keywords:** quantum chromodynamics, 3D imaging, transverse momentum distributions, parity violation deep inelastic scattering, standard model, proton gluonic gravitational form factors,  $J/\psi$  electro- and photoproduction

(Some figures may appear in colour only in the online journal)

**1. Executive summary**

To exploit the full potential of the 12 GeV energy upgrade of the continuous electron beam accelerator facility (CEBAF) at Jefferson Lab (JLab), we have designed a new spectrometer, named the solenoidal large intensity device (SoLID) [1, 2]. The main feature of SoLID is its large acceptance and the capacity to operate at the full CEBAF luminosity of up to  $10^{39} \text{ cm}^{-2} \text{ s}^{-1}$ . A rich and diverse science program consisting of a set of high impact physics experiments has been developed with SoLID. The SoLID proposal was submitted as a major item of equipment to the U.S. Department of Energy (DOE) and after passing several Director's Reviews at JLab, received a successful Science Review from the DOE in March 2021. We are presently awaiting the full report describing the review outcome.

The SoLID spectrometer fills a critical void in the science reach of quantum chromodynamics (QCD) and fundamental symmetry studies. For illustration, figure 1 shows the acceptance and luminosity range covered by JLab, the electron-ion collider (EIC), and a number of lower-luminosity facilities that were designed to investigate the properties of quarks and gluons in the nucleon and their modified behavior in nuclei. To maximize physics insight, it is essential to explore reactions over as large a range of  $Q^2$  and Bjorken  $x$  as possible. Together, JLab and the EIC will, over the next several decades, cover a broad and largely complementary kinematic range, with SoLID probing key physics and providing precision data primarily in the high- $x$  region.

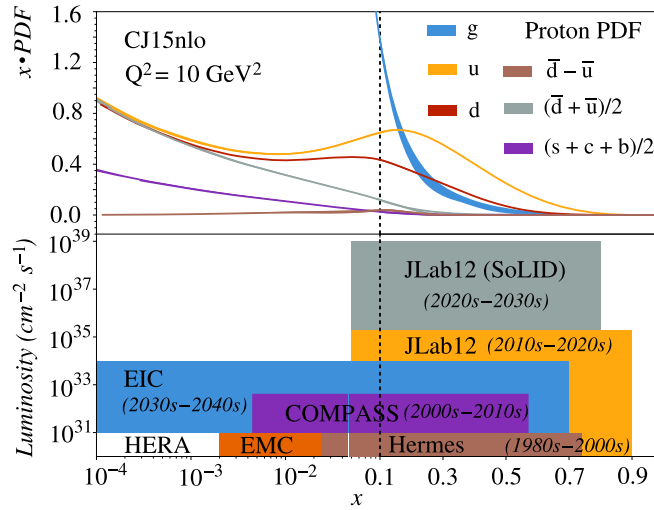


**Figure 1.** Landscape of the QCD program. SoLID expands the luminosity frontier in the large  $x$  region whereas the EIC does the same for low  $x$ . Reproduced with permission from [3].

SoLID can accommodate a variety of experimental configurations for a broad spectrum of physics. Five primary experiments have been approved with the highest rating (‘A’) by the JLab Program Advisory Committee (PAC). Three of these are measurements of transverse-momentum-dependent distributions (TMDs) describing the three-dimensional structure of the nucleon in momentum space via semi-inclusive deep inelastic scattering (SIDIS) with polarized  $^3\text{He}$  and proton targets [4–6]. The fourth aims at understanding the origin of the proton mass via measurements of near-threshold photo-production and electroproduction of the  $J/\psi$  meson [7]. The final one will test the electroweak sector of the Standard Model at low energy and study hadronic physics in the high- $x$  region [8] through measurements of Parity-Violating Deep Inelastic Scattering (PVDIS). In July 2022, two further experiments were approved, one to study the flavor dependence of the EMC effect using PVDIS with a  $^{48}\text{Ca}$  target [9] and the other to study hadronic physics with two-photon exchange (TPE) via a measurement of the beam-normal single-spin asymmetry in DIS [10]. In addition, a series of approved experiments will run simultaneously with the main experiments. These include deep exclusive meson production (DEMP) [11] and time-like Compton scattering (TCS) [12], which access the generalized parton distributions (GPDs) and improve our knowledge of the spatial three-dimensional structure of the nucleon.

The SoLID spectrometer can operate at such high luminosity in large part due to recent developments in detectors, data acquisition, and computing technologies. High-rate tracking detectors such as gas electron multipliers (GEMs), Cherenkov counters with advanced photon detectors, and fast multi-gap resistive plate chambers (MRPCs) for TOF measurements are key examples. Fast electronics developed at JLab will handle the high trigger and background rates. The large data volume can be handled by the advanced computing facility at JLab. These technological advancements, not available in the initial planning stages of the 12 GeV program, have become a reality and allow us to fully exploit the available accelerator capabilities to advance the frontiers of QCD studies.

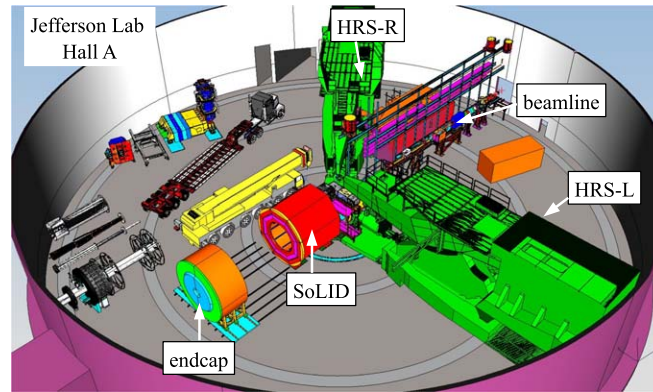


**Figure 2.** Schematic layout of SoLID in Hall A, with the endcap pulled downstream to allow detector installation and reconfiguration. The two high-resolution spectrometers (HRS-L and HRS-R, not in use) are parked at backward angles.

## 2. Introduction

Since commencing operation in 1995, CEBAF has been the medium-energy electron scattering facility with the worldwide highest luminosity for conducting experiments with fixed proton and nuclear targets. Initially delivering electron beams with energies of up to 6 GeV, CEBAF was successfully upgraded in 2017, raising the beam energy to 12 GeV. Along with the energy upgrade, another experimental hall, Hall D, was added to the facility, and detectors in the other experimental halls were improved. At the same time, JLab's physics program has evolved to match the progress in our understanding of the structure of the nucleon within the theory of the strong interaction, known as QCD, and to push for higher precision in measurements of fundamental symmetries. Progress on both these frontiers requires first and foremost higher statistics. QCD studies aim to describe nucleon structure in three dimensions in both momentum and coordinate space using SIDIS and deeply virtual exclusive processes. Obtaining the desired 3D mapping involves dividing the experimental data into many multi-dimensional bins, which is only meaningful if the total data set contains a very large number of events. Meanwhile, decades of experience in improving systematic uncertainties of parity-violating electron scattering (PVES) experiments allow us to measure spin-dependent asymmetries in DIS with a precision of better than parts per million (ppm), which calls for event counts of order  $10^{12}$ . Similarly,  $J/\psi$  production on the proton requires high luminosity so that a sufficient number of events can be accumulated near the production threshold, where the cross section falls rapidly.

SoLID is designed to fulfill these needs. By combining a 1.4 T solenoid magnet and a large-acceptance detector that covers  $2\pi$  azimuthal angle, SoLID is particularly suitable to collect data with high statistics from DIS, SIDIS and Deep-Virtual exclusive processes. In addition, the SoLID design fully incorporates the ability to reconfigure all detector systems in order to optimize detection capabilities for SIDIS and  $J/\psi$  meson production on the one hand, and for the PVDIS program on the other. SoLID is intended to be installed in experimental Hall A, as shown in figure 2.

In SIDIS, both a hadron and the scattered primary electron are detected in the final state. The SIDIS process probes the distributions of quarks as a function of their transverse momentum and transverse spin. These distributions are the transverse-momentum-dependent parton distributions (TMDs). At the leading twist, there are eight independent TMDs. All of

them can be extracted from SIDIS experiments with different combinations of target/beam polarization and angular modulations. There are three approved SoLID SIDIS experiments, including two on a  $^3\text{He}$  target: one with a longitudinal polarization [5], and the other with a transverse polarization [4]. The third experiment will use a transversely polarized proton target [6].

For SIDIS, the relevant variables are  $P_T$ , the hadron transverse momentum,  $z$ , the fraction of longitudinal momentum carried by the hadron, and  $Q^2$  and  $x$  which are characteristic of the inclusive DIS process. Thus the SIDIS process to extract TMDs has multi-variable dependence, and a large data set is required to attain good statistics without integrating over one or more of the variables. This is the main reason the high luminosity of the SoLID spectrometer is required.

The main goal of the proposed SoLID  $J/\psi$  measurement is to study the gluonic field contributions to the proton structure and proton mass. Gluons play an essential role in the structure of the proton, which is evident from the difference between the proton's total mass and its constituents' current quark masses. Most of the proton information carried by the gluons can be encoded in three gravitational form factors dubbed  $A_g$ ,  $B_g$  and  $C_g$  that are part of the matrix element of the QCD energy-momentum tensor. A compelling way to access these form factors is through virtual heavy-meson photo- and electro-production over the widest possible range of photon-nucleon invariant mass. Following recent studies, the region near the  $J/\psi$  production threshold seems to be a very promising kinematic sector, not only for obtaining these form factors and thus determining the mass and scalar radius (dominated by gluons) of the proton, but also for exploring the trace anomaly that underlies the origin of the proton mass.

As a consequence, extensive data are required very close to threshold, where the cross section is very small. The large acceptance of SoLID and its ability to handle high luminosity make it the ideal detector to study this physics with threshold  $J/\psi$  production [7]. The EIC will provide complementary information through the production of the higher-mass  $\Upsilon$  particle. Since extraction of the gluonic form factors are model independent, measurements at both facilities agreeing with lattice QCD will give strong confidence in the interpretation.

The goal of the SoLID PVDIS program [8] is to measure the cross section asymmetry,  $A_{PV}$ , between right- and left-handed beam electrons with high precision. This asymmetry originates from parity non-conservation in weak interactions. At JLab energies, it can be determined from the interference between photon and  $Z^0$  exchange processes in DIS. SoLID will provide data on  $A_{PV}$  with sub-percent relative precision over a wide ( $x$ ,  $Q^2$ ) range. Measured on a deuteron target, the  $A_{PV}^{(d)}$  data can be used to determine parameters of the electroweak Standard Model and to set limits on new physics up to an energy scale that is comparable to the reach of the LHC. The SoLID PVDIS deuteron measurement is unique in that it measures the strength of a particular contact interaction, the effective electron-quark VA couplings, that cannot be isolated by any other experiments at present. Measured on a proton target,  $A_{PV}^{(p)}$  can help determine the parton distribution function (PDF) ratio  $d/u$  at large  $x$  without nuclear effects. Lastly, PVDIS asymmetries can probe specific hadronic physics effects such as charge symmetry violation (CSV). CSV at the quark level would be reflected in a specific kinematic dependence of the deuteron asymmetry, while effects of CSV at the nuclear level can be studied by measuring PVDIS asymmetries on a nuclear target such as  $^{48}\text{Ca}$  [9].

With SoLID being a versatile spectrometer, many other processes can be measured. The full azimuthal coverage of SoLID allows for the determination of the beam-normal single-spin asymmetry to high precision in DIS [10], providing a new observable for studying two-photon-exchange effects. A number of run-group experiments will collect data at the

same time as the SIDIS and  $J/\psi$  experiments, including some that aim at studying GPDs [11, 12].

This paper is organized as follows: the SIDIS, PVDIS, and  $J/\psi$  programs are described in sections 3–5, respectively. In section 6 we expand on the GPD program (both approved run-group experiments and key measurements under study) with SoLID, and in section 7 all other run-group experiments, the beam-normal single-spin-asymmetry (BNSSA) experiment, and an idea to measure PVDIS asymmetry using a polarized target. The SoLID instrumentation is detailed in section 8. Finally, in section 9, we discuss unique measurements that will become possible should a positron beam or an energy upgrade of CEBAF be realized in the future.

### 3. Semi-inclusive deep inelastic scattering

#### 3.1. The three-dimensional momentum structure of the nucleon

A substantial amount of our knowledge of the internal structure of nucleons and nuclei in terms of quarks and gluons, the fundamental degrees of freedom of QCD, has been obtained through experimental and theoretical studies of the PDFs [13] and fragmentation functions (FFs) [14]. Within the collinear factorization scheme of deep inelastic lepton–nucleon scattering (DIS), leading-twist integrated PDFs are defined as probability densities for finding an unpolarized or longitudinally polarized parton in a fast-moving unpolarized or longitudinally polarized nucleon (‘longitudinal’ is defined as along the nucleon moving direction). These PDFs depend on two variables 4-momentum transfer-squared,  $Q^2$ , and longitudinal momentum fraction,  $x$ . The dependence on  $Q^2$  is due to gluon radiations and is governed by the QCD evolution equation. These PDFs are considered to be one-dimensional, i.e. they depend only on the longitudinal momentum and are well-investigated. On the other hand, over the past two decades, the frontier of studies has moved forward to include three-dimensional PDFs, which describe the partonic motion and spatial distributions in the transverse direction, i.e. perpendicular to the nucleon’s momentum.



Semi-inclusive deep inelastic scattering (SIDIS) of leptons off nucleons, in which the scattered lepton and a leading hadron are detected in the final state, is a powerful tool to probe the transverse momentum and spin structure of the nucleon in addition to the longitudinal structure. Through this process, one can extract the transverse-momentum-dependent parton distribution functions (TMD-PDFs or just TMDs), which permit a three-dimensional tomography of the nucleon in momentum space. Through exclusive processes such as deeply virtual Compton scattering, one can extract different views of nucleon through generalized parton distribution functions (GPDs), where the three dimensions are the longitudinal momentum and the two spatial coordinates in the transverse plane. All the information on TMDs and GPDs is contained in the five-dimensional Wigner distribution functions [15, 16]. The study of TMDs on the partonic structure of the nucleon in three-dimensional momentum space probes rich non-perturbative QCD dynamics and phenomena, and provides essential information on partonic orbital motion and spin–orbit correlations inside the nucleon. In addition, TMDs cast light on multi-parton correlations at the leading twist, which helps uncover the dynamics of the nucleon’s quark–gluon structure.

#### 3.2. TMDs and spin asymmetries

Most TMDs stem from the coupling of the quark transverse momentum to the spin of the nucleon and quark. Hence, one can study spin–orbit correlations in QCD with TMDs. At leading twist, if one integrates over the quark transverse momenta inside the nucleon, the



**Leading Twist TMDs**

 : Nucleon Spin    
  : Quark Spin

		Quark polarization		
		Un-Polarized (U)	Longitudinally Polarized (L)	Transversely Polarized (T)
Nucleon Polarization	U	$f_1 = \odot$		$h_1^\perp = \uparrow - \downarrow$ Boer-Mulder
	L		$g_1 = \rightarrow - \leftarrow$ Helicity	$h_{1L}^\perp = \rightarrow - \leftarrow$ Worm gear
	T	$f_{1T}^\perp = \uparrow - \downarrow$ Sivers	$g_{1T}^\perp = \uparrow - \downarrow$ Worm gear	$h_{1T}^\perp = \uparrow - \downarrow$ Pretzelosity

**Figure 3.** Eight leading-twist TMDs arranged according to the quark ( $f$ ,  $g$ ,  $h$ ) and nucleon (U, L, T) polarizations. Figure from [2].

surviving TMDs are the unpolarized parton distribution  $f_1$ , the longitudinally polarized parton distribution  $g_1$  (helicity), and the transversely polarized quark distribution function  $h_{1T}$  (transversity) [17]. In addition to  $f_1$ ,  $g_1$ , and  $h_{1T}$ , there are five additional leading-twist TMDs [18, 19], some of which vanish in the absence of quark orbital angular momentum (OAM). Figure 3 tabulates these eight TMDs according to quark and nucleon polarization, where U, L, and T denote unpolarized, longitudinal, transverse polarization, respectively. All are functions of the longitudinal momentum fraction  $x$  (Bjorken  $x$ ) and the quark transverse momentum  $\mathbf{k}_\perp$ .

Let us focus on the following TMDs shown in figure 3: transversity, pretzelosity, Sivers, and worm-gear. Also given are the dependence on nucleon spin  $\mathbf{S}_T$ , quark spin  $\mathbf{s}_q$ , and virtual photon three-momentum  $\mathbf{P}$ , which defines the longitudinal,  $z$ , direction.

- (i) **Transversity TMD**, depending on  $\mathbf{S}_T \cdot \mathbf{s}_q$ : in the parton model, provides information on the probability of finding transversely polarized quarks (anti-quarks) in a transversely polarized nucleon. Due to relativistic effect, the transversity TMD behaves differently from the helicity TMD, which provides information on the probability of finding longitudinally polarized quarks (anti-quarks) in a longitudinally polarized nucleon. The integral of transversity over  $x$  yields the tensor charge [20–22], which is an important property of the nucleon that has been calculated precisely by lattice QCD. Precise measurements of the tensor charges of the proton and neutron will allow for their quark flavor separation and provide direct comparisons to lattice QCD predictions. Quark tensor charges are coefficients for the quark electric dipole moments (EDMs) to connect to nucleon EDMs if nucleon EDMs originate from quark EDMs, making them important for tests of the Standard Model (SM) and searches for new physics beyond the SM.
- (ii) **Pretzelosity TMD**, depending on  $\mathbf{S}_T \cdot [\mathbf{k}_\perp \mathbf{k}_\perp] \cdot \mathbf{s}_{qT}$ , describes the correlation among the transverse spin of the nucleon, transverse spin of the quark, as well as the transverse motion of the quark inside the nucleon. The pretzelosity distribution reflects the difference between helicity and transversity TMDs. This difference is due to relativistic effects. In various quark and QCD-inspired models, pretzelosity TMD has been shown to provide quantitative information about the OAM of the partons inside the nucleon.
- (iii) **Sivers TMD**, depending on  $\mathbf{S}_T \cdot \mathbf{k}_\perp \times \mathbf{P}$ , describes a correlation between the nucleon transverse spin and the quark orbital motion.



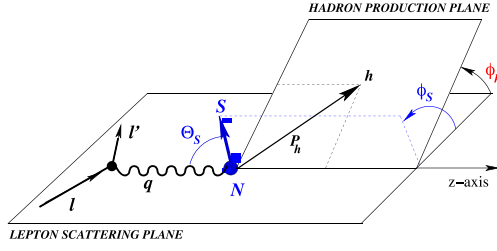


**Figure 4.** Kinematics of SIDIS in the one-photon exchange approximation. Reproduced from [23]. CC BY 4.0.

The Sivers TMD would vanish if there were no parton OAM. Hence, studies of Sivers TMD help understand the contribution of the quark OAM to the nucleon spin. Another interesting aspect is the predicted sign change between the Sivers function extracted from SIDIS process versus that from the Drell-Yan process based on QCD. The experimental test of such a sign change has been another important motivation for the study of the Sivers TMD.

- (iv) **Worm-gear TMDs**,  $g_{1T}$  and  $h_{1L}^\perp$ , are twist-2 TMD PDFs related to the transverse motion of quark, nucleon spin, and quark spin. They are also known as ‘worm-gear’ functions since they link perpendicular spin configurations between the nucleon and quarks. More specifically,  $g_{1T}$  describes the distribution of a longitudinally polarized quark inside a transversely polarized nucleon, while  $h_{1L}^\perp$  describes the distribution of a transversely polarized quark inside a longitudinally polarized nucleon. Interestingly, the worm-gear functions cannot be generated dynamically from coordinate space densities by final state interactions, and thus have no analogous terms in impact parameter (coordinate) space described by GPDs. Their appearance is a sign of intrinsic transverse motion of quarks.

Figure 4 illustrates the SIDIS process in terms of the azimuthal angles defined with respect to the lepton scattering plane.  $\phi_h$  is the angle between the lepton scattering plane and the hadron production plane, while  $\phi_S$  is the angle between the lepton scattering plane and that defined by the polarization vector of the target’s spin and the virtual photon three-momentum vector.

In SIDIS of unpolarized leptons from transversely polarized nucleons, the target single-spin asymmetries (SSAs) allow one to experimentally explore the three aforementioned TMDs—transversity, pretzelosity and sivers—through various azimuthal angular dependencies.

In the leading twist formalism, the SSAs can be written with these three leading twist terms as:

$$A_{UT} = A_{UT}^{\text{Collins}} \sin(\phi_h + \phi_S) + A_{UT}^{\text{Pretzelosity}} \sin(3\phi_h - \phi_S) + A_{UT}^{\text{Sivers}} \sin(\phi_h - \phi_S). \quad (1)$$

Here in  $A_{UT}$ , the first subscript U (or L) refers to the unpolarized beam (or longitudinally polarized beam). The second subscript T (or U, or L) refers to the target, which is transversely polarized (or unpolarized, or longitudinally polarized) with respect to the virtual photon three-momentum vector. The SSAs in equation (1) are represented as follows, assuming TMD factorization holds:

$$(i) \quad A_{UT}^{\text{Collins}} \propto \langle \sin(\phi_h + \phi_s) \rangle_{UT} \propto h_{1T} \otimes H_1^\perp, \quad (2)$$

where,  $H_1^\perp$  is the Collins FF [24], extracted from charged pion pair production based on  $e^+e^-$  annihilation [25],  $\otimes$  represents a convolution.

$$(ii) \quad A_{UT}^{\text{Pretzelosity}} \propto \langle \sin(3\phi_h - \phi_s) \rangle_{UT} \propto h_{1T}^\perp \otimes H_1^\perp, \quad (3)$$

where  $h_{1T}^\perp$  is the pretzelosity TMD, and the same Collins FF appears. Models show that non-zero pretzelosity requires interference between the nucleon wave function components differing by two units of OAM of the quarks (e.g. the interference of the  $p$ - $p$  or  $s$ - $d$  OAM states). The Pretzelosity asymmetry stems from quarks that are polarized perpendicularly to the nucleon spin direction, in the transverse plane within a transversely polarized nucleon.

$$(iii) \quad A_{UT}^{\text{Sivers}} \propto \langle \sin(\phi_h - \phi_s) \rangle_{UT} \propto f_{1T} \perp \otimes D_1, \quad (4)$$

where  $f_{1T}$  is the Sivers function, describing the probability density of finding unpolarized quarks inside a transversely polarized nucleon, and  $D_1$  is the unpolarized FF.

These three asymmetries are part of the total 18 terms in the SIDIS differential cross section expression [23]. There are five terms depending on target transverse spin direction  $S_T$ . Two of the five terms are higher-twist terms. At leading twist, only the following three terms are relevant for the target transverse single spin asymmetry:

$$\begin{aligned} \frac{d\sigma_{\text{SIDIS}}}{dx dy dz dP_{h\perp}^2 d\phi_h d\phi_s} &= \frac{\alpha^2}{xyQ^2} \left( 1 - y + \frac{1}{2}y^2 \right) F_{UU}(x, y, P_{h\perp}^2) \{ 1 + \dots + S_T \sin(\phi_h + \phi_s) \\ &\quad \times p_1 A_{UT}^{\text{Collins}} + S_T \sin(3\phi_h - \phi_s) p_1 A_{UT}^{\text{Pretzelosity}} + S_T \sin(\phi_h - \phi_s) A_{UT}^{\text{Sivers}} + \dots \}. \end{aligned} \quad (5)$$

For definitions of the kinematic variables and the coefficient  $p_1$ , see equations (2.1) and (2.3) in [23].

These SIDIS SSAs depend on four kinematic variables that are  $(x, P_{hT}, z, Q^2)$ , and such asymmetries are typically small and kinematic dependent. Therefore, high-precision measurements of these asymmetries in such a 4D kinematic space will require a *large acceptance* + *high luminosity* device (such as SoLID) with a full azimuthal angular range to disentangle various azimuthal angular dependencies.

The experimental SSA for a detector such as SoLID with a full  $2\pi$  azimuthal angular acceptance is defined as [4]

$$A_{UT}(\phi_h, \phi_s) = \frac{2}{P_T^1 + P_T^2} \times \frac{\sqrt{N_1 \uparrow N_2 \downarrow} - \sqrt{N_1 \downarrow N_2 \uparrow}}{\sqrt{N_1 \uparrow N_2 \downarrow} + \sqrt{N_1 \downarrow N_2 \uparrow}}. \quad (6)$$

In this formula, the given number of counts  $N_1 \uparrow \equiv N_1(\phi_h, \phi_s)$  and  $N_1 \downarrow \equiv N_1(\phi_h, \phi_s + \pi)$  are taken at the same time while the target polarization is  $P_T^1$ .  $N_2 \uparrow \equiv N_2(\phi_h, \phi_s)$  and  $N_2 \downarrow \equiv N_2(\phi_h, \phi_s + \pi)$  are taken at the same time with the target polarization being  $P_T^2$ , when the target spin is flipped by  $180^\circ$ .

The JLab PAC50 in July 2022 reviewed all SoLID SIDIS experiments and reaffirmed their importance and re-approved all SIDIS experiments with the highest scientific rating of ‘A’. SoLID’s full  $2\pi$  azimuthal angular coverage has a unique advantage in reducing systematic uncertainties associated with flipping the target spin direction apart from those associated with luminosity and detection efficiencies.

While we use these three SSAs to illustrate how one can access information concerning certain TMDs from SIDIS processes, we point out that all eight leading-twist TMDs can be accessed through various lepton and nucleon polarization combinations from SIDIS processes. For example, the aforementioned worm-gear function,  $g_{1T}$ , can be accessed through

the beam-target double-spin asymmetry (DSA) of  $A_{LT}$  with an azimuthal angular modulation of  $\cos(\phi_h - \phi_S)$ . Such DSA measurements require a longitudinally polarized lepton beam and a transversely polarized target, as was used in [26]. The other worm-gear piece,  $h_{1L}^\perp$ , and helicity  $g_{1L}$  can be accessed with a longitudinally polarized target through SSA and DSA measurements of  $A_{UL}$  (with an angular modulation of  $\sin 2\phi_h$ ) and  $A_{LL}$ , respectively. For details, we refer to a recent review article [27].

### 3.3. The SoLID SIDIS program

The 12 GeV physics era at JLab opens a great new window to accomplish precision studies of the transverse spin and TMD structure of the nucleon in the valence quark region. The experimental program on TMDs is one of the science pillars of the 12 GeV program at JLab. The SoLID SIDIS program aims to address the following questions.

- Is it possible to precisely determine the tensor charge of the  $u$  and  $d$  quarks, which are fundamental properties of the nucleon?  
The tensor charge of the  $u$  and  $d$  quarks can be determined to a high precision from the SoLID SIDIS program. They will provide a precision test of lattice QCD calculations.
- How do we quantify the quark transverse motion inside the nucleon and observe spin-orbit correlations?  
The Sivers TMD has been predicted in a variety of models to have the sensitivity to spin-orbit correlations and can provide quantitative information about the transverse motion of the quarks inside the nucleon. With the kinematic reach of SoLID at 12 GeV and the precision SoLID measurements will have, the SoLID SIDIS program will answer the above question and also determine whether the confined motion in the transverse plane is dependent on Bjorken  $x$  in the valence quark region.
- Is it possible to provide quantitative information on the quark OAM?  
Based on the previous discussion, both Sivers and pretzelosity TMDs are able to provide quantitative information on the quark OAM.
- Are there clear signatures for relativistic effect inside the nucleon and can we observe them?

Both transversity and pretzelosity TMDs will provide clear and quantitative information about relativistic effects inside the nucleon. The transverse TMD would be the same as that of the helicity TMD if it were not for the relativistic effect. The relation among the helicity, the transversity and the pretzelosity TMDs provides another signature for the relativistic effect inside the nucleon. Again with the high-precision SoLID will achieve, this question will be answered.

In summary, these questions will be answered by three “A”-rated SoLID experiments approved by the JLab PAC [4–6], along with two run group experiments [28, 29]. Recently the JLab PAC50 in July 2022 reviewed these experiments and reaffirmed their importance. These new experiments will employ a superconducting solenoid magnet, a detector system consisting of forward-angle and large-angle sub-detectors, as well as a high-pressure transversely/longitudinally polarized  $^3\text{He}$  (neutron) target and a transversely polarized  $\text{NH}_3$  (proton) target, positioned upstream of the magnet. In order to extract TMDs with precision from SSA and DSA measurements, the SoLID detection system will have the capability of handling large luminosities with a large acceptance, a full azimuthal angular coverage, good kinematic coverage in terms of the  $x$ ,  $P_{hT}$ ,  $z$ ,  $Q^2$  variables for SIDIS, and good particle identification for electrons and charged pions and kaons.

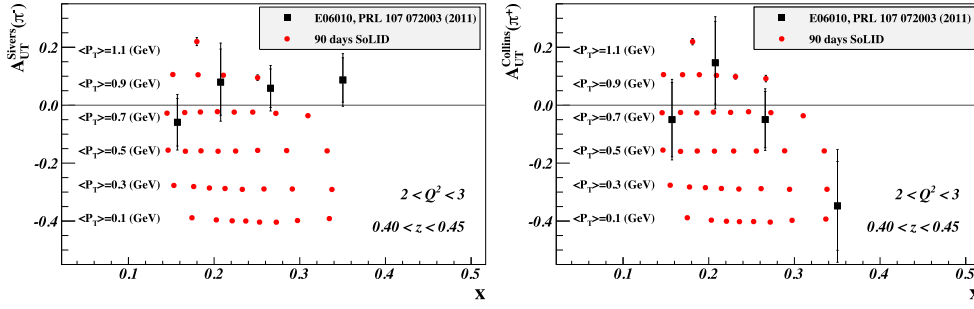


**Figure 5.** The left panel shows the projected Siverts asymmetry measurement for  $\pi^-$  for a typical  $z$  and  $Q^2$  bin ( $0.40 < z < 0.45$ ,  $2 \text{ GeV}^2 < Q^2 < 3 \text{ GeV}^2$ ) as a function of  $x$ , with different ranges of the hadron  $P_{hT}$  labeled. In the plots  $P_{hT} = P_T$ . The right panel shows the projected Collins asymmetry measurement for  $\pi^+$  in the same binning. Also shown are the results from the 6 GeV experiment E06-010 [30]. Both plots are from [1]. Reproduced with permission from [1].

### The three approved SIDIS experiments

*Experiment E12-10-006* [4] with a transversely polarized  $^3\text{He}$  target: the experiment E12-10-006 has been approved for 90 d of total beam time with 15  $\mu\text{A}$ , 11/8.8 GeV electron beams on a 40 cm long, 10 amgs (1 amg = 1 atm at 0 °C) transversely polarized  $^3\text{He}$  target. The projected data from E12-10-006 are binned in  $(x, P_{hT}, z, Q^2)$  space, and only SoLID allows for such 4D binning with excellent precision for each bin. As examples, for a typical  $z$  and  $Q^2$  bin ( $0.40 < z < 0.45$ ,  $2 \text{ GeV}^2 < Q^2 < 3 \text{ GeV}^2$ ), data projections for the Siverts and Collins asymmetry measurements are shown in figure 5 with the left panel for the Siverts  $\pi^-$  and right panel for the Collins  $\pi^+$  asymmetries. For the complete projections, which consist over 1400 data points, we refer to the proposal [4].

*Experiment E12-11-007* [5] with a longitudinally polarized  $^3\text{He}$  target: the experiment E12-11-007 has been approved for 35 d of total beam time with 15  $\mu\text{A}$ , 11/8.8 GeV electron beams on a 40 cm long, 10 amgs longitudinally polarized  $^3\text{He}$  target to match about 50% statistics of the experiment E12-10-006. The projected data are binned into  $(x, P_{hT}, z, Q^2)$  bins. For a typical  $z$  and  $Q^2$  bin ( $0.40 < z < 0.45$ ,  $2 \text{ GeV}^2 < Q^2 < 3 \text{ GeV}^2$ , one of the total 48  $z$ - $Q^2$  slices), data projections are shown in figure 6 as examples. For the complete projections, we refer to the proposal [5].

*Experiment E12-11-108* [6] with a transversely polarized  $\text{NH}_3$  target: The experiment E12-11-108 has been approved for 120 d with 100 nA, 11/8.8 GeV electron beams on a 3 cm long, polarized  $\text{NH}_3$  target. The 8.8 GeV beam energy will provide precision data for radiative corrections along with the increased  $Q^2$  coverage. The projected data from E12-11-108 are binned into  $(x, P_{hT}, z, Q^2)$  bins. As an example, for a typical  $z$  and  $Q^2$  bin ( $0.40 < z < 0.45$ ,  $2 \text{ GeV}^2 < Q^2 < 3 \text{ GeV}^2$ ), data projections for the Collins asymmetry measurements are shown in figure 7 with the left panel for  $\pi^+$  and right panel for  $\pi^-$ . For the complete projections of E12-11-108, we refer to the proposal [6].

In July 2022 these three SoLID SIDIS proposals were presented to the JLab PAC50 as part of the JLab jeopardy review process. The PAC reaffirmed the importance of the program and all three experiments remain active with ‘A’ rating. The PAC evaluation summary for each of the three SIDIS experiments is quoted here “This experiment will provide data of unprecedented quality on SIDIS in JLab-12 GeV kinematics. The theory and phenomenology developments in the last decade make this experiment yet more compelling and highlight the impact of SoLID program.”

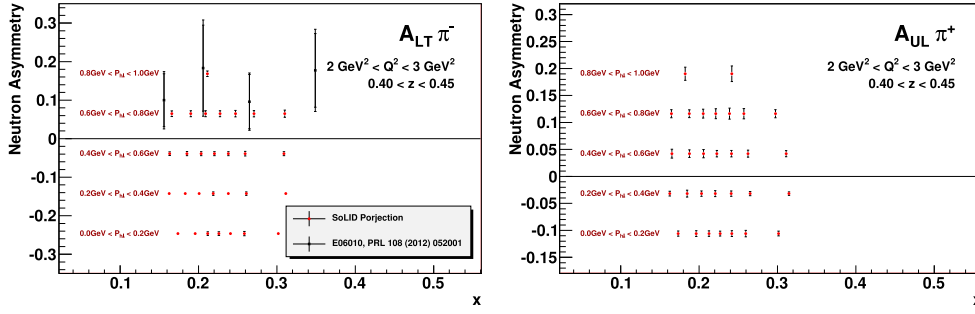


**Figure 6.** The left panel shows the projection for a typical  $z$  and  $Q^2$  bin ( $0.40 < z < 0.45$ ,  $2 \text{ GeV}^2 < Q^2 < 3 \text{ GeV}^2$ ) for the  $\pi^+$  single-target spin asymmetry  $A_{UL}^{\sin(2\Phi_h)}$  measurement as a function of  $x$ , with different ranges of the hadron  $P_{hT}$  labeled. In the plots  $P_{hT} = P_T$ . The right panel shows the projection for the corresponding  $z$ - $Q^2$  bin for the  $\pi^-$  double-target spin asymmetry  $A_{LT}^{\cos(\Phi_h - \Phi_S)}$  measurement. Also shown are the results from the 6 GeV experiment E06-010 [26].

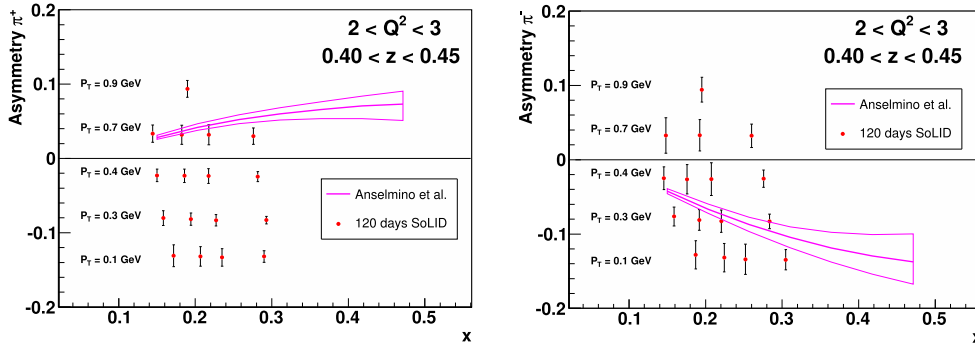


**Figure 7.** The left panel shows the projection for a typical  $z$  and  $Q^2$  bin ( $0.40 < z < 0.45$ ,  $2 \text{ GeV}^2 < Q^2 < 3 \text{ GeV}^2$ ) for the  $\pi^+$  Collins asymmetry measurement as a function of  $x$ , with different ranges of the hadron  $P_{hT}$  labeled. In the plots  $P_{hT} = P_T$ . The right panel shows the projection for the corresponding  $z$ - $Q^2$  bin for the  $\pi^-$  measurement. Also shown are the predictions of the Collins asymmetry from Anselmino *et al* [31] with model uncertainties.

### The SIDIS run group experiments

*Di-hadron electroproduction in DIS with transversely polarized  $^3\text{He}$  target at 11 and 8.8 GeV* [28]: a study of transversity parton distribution using measurements of semi-inclusive electroproduction of two charged pions in the DIS region will be carried out. The data will provide input to extract the  $u$  and  $d$  transversity distributions in a model-independent way. This experiment will be run in parallel with the approved experiment E12-10-006.

*$K^\pm$  production in SIDIS using transversely polarized targets and the SoLID spectrometer* [29]: a study of measurements of  $K^\pm$  production in SIDIS using both the transversely polarized  $^3\text{He}$  and  $\text{NH}_3$  targets will be performed, to extract the  $K^\pm$  Collins, Sivers and other TMD asymmetries. The data will provide input to determine the  $u$ ,  $d$  and sea quarks' TMDs. This experiment will be run in parallel with the approved experiments E12-10-006 and E12-11-108.

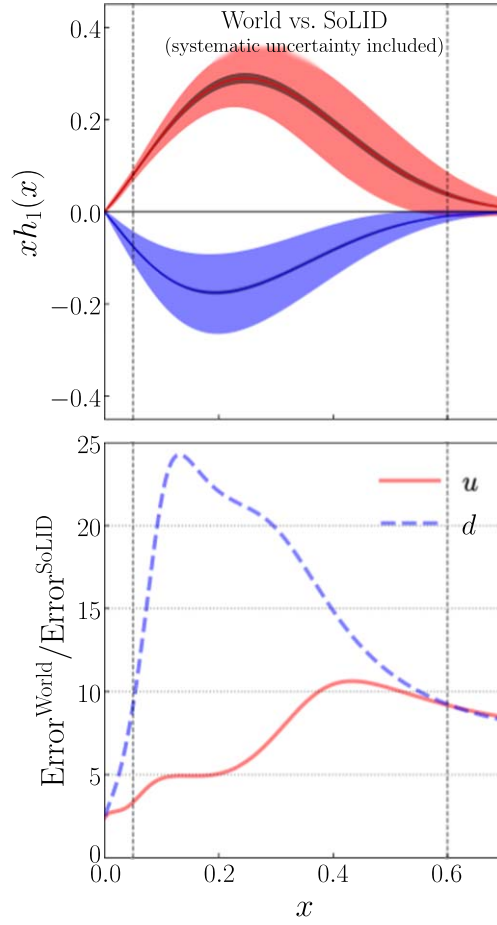


**Figure 8.** The impact on the  $u$  and  $d$  quarks' transversity distributions by the SoLID SIDIS program. In the top panel, the wide uncertainty bands show our current knowledge from the world data global analysis, whereas the narrow uncertainty bands show the SoLID projections. The bottom panel shows the improvements, manifested in the ratios between the current and projected uncertainties.

More details on these two run group experiments will be given in section 7.

### 3.4. Transversity, tensor charge, and EDM

The combination of the SIDIS experiments discussed above will give an opportunity for accessing essential information on TMDs from the neutron and the proton in the valence quark region, and for flavor separation of TMDs (e.g. transversity, pretzelosity, sivers and  $g_{1T}$ ) for  $u$  and  $d$  quarks. Figure 8 shows the projected SoLID transversity distributions for the  $u$  and  $d$  quarks at a typical value of  $Q^2 = 2.4 \text{ GeV}^2$  obtained with our up-to-date knowledge of evolution of TMDs and FFs, including both systematic and statistical uncertainties. The  $x$ -range between the two vertical dashed lines is directly measurable by SoLID. The precision data in the valence quark region will make a major improvement in our knowledge of the transversity distribution. The program will also allow us to study the  $k_T$  dependence and the  $Q^2$  evolution of TMDs.

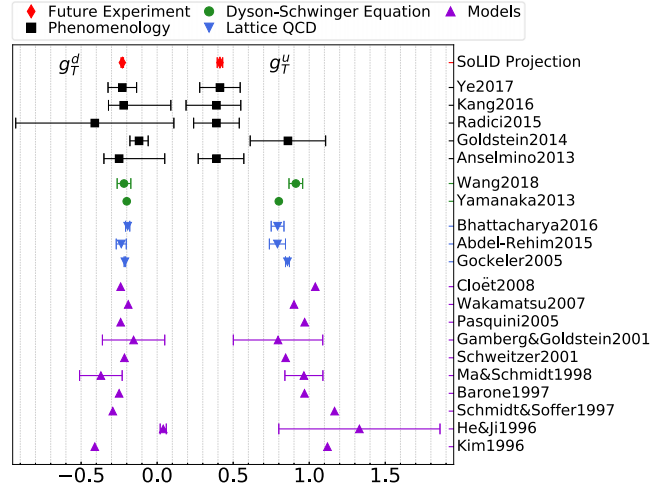


**Figure 9.** The impact of the projected SoLID measurement of the down (left) and up (right) quark tensor charges (see equation (7)) together with the current knowledge from various models, Dyson–Schwinger equations, global analyzes, and lattice QCD simulations.

Moreover, we will obtain precise information on the quark tensor charge defined as

$$g_T^q = \int_0^1 [h_1^q(x) - h_1^{\bar{q}}(x)] dx. \quad (7)$$

The nucleon (quark) tensor charge is as important as its electric charge, mass and spin. It has been calculated by lattice QCD and the prediction is becoming increasingly precise. It is also an input for the tests of the Standard Model (see below). A quantitative study in [32] shows that the SoLID SIDIS program will improve the accuracy of the tensor charge determination by one order of magnitude, allowing for a benchmark test of lattice QCD predictions. The high impact of the SoLID projections on the extraction of the tensor charge of the  $u$  and  $d$  quarks is demonstrated in figures 9 and 10. The projected SoLID  $u$  and  $d$  quark tensor charges are  $g_T^u = 0.547 \pm 0.021$ ,  $g_T^d = -0.376 \pm 0.014$ . They represent less than 4% relative uncertainty for the SoLID extraction of the  $u$  and  $d$  quark tensor charge, and should be compared to the 2019 FLAG review [33] of the Lattice QCD calculations where the corresponding numbers are 4% and 7% for  $u$  and  $d$  quark, respectively. The Lattice QCD calculations [34, 35] of isovector tensor charge reached precision of 3%. Therefore, these results will provide a benchmark test of precise lattice calculations.

More recent global analysis and extraction of the tensor charge by the JAM collaboration included world data and Lattice QCD results [36, 37]. Their extracted tensor charges of the  $u$  and  $d$  quarks are shown in 2D plot in figure 10, along with the SoLID projection. The JAM collaboration also made projections [38] for both SoLID and EIC, concluded that combining both would lead to the most precise extractions of the tensor charge.

The tensor charge is also connected to the neutron and proton electric dipole moments (EDMs), giving us a unique opportunity to test the Standard Model (SM) and to search for new physics beyond SM. The nucleon EDM is related to the quark EDM as [39–42]:

$$d_p = g_T^u d_u + g_T^d d_d + g_T^s d_s \quad (8)$$



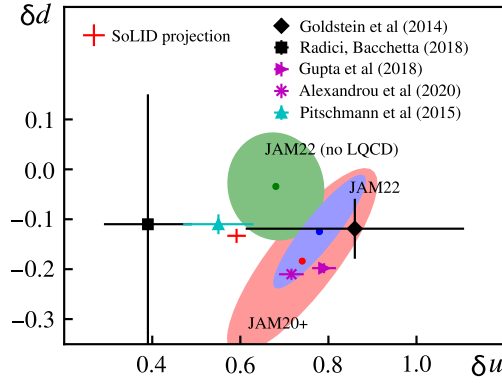


**Figure 10.** The impact of the projected SoLID measurement of the tensor charge added to the left panel of figure 3 of [36] with the vertical axis showing the  $d$ -quark tensor charge and the horizontal axis showing the  $u$ -quark tensor charge. Reproduced from [36]. CC BY 4.0.

$$d_n = g_T^d d_u + g_T^u d_d + g_T^s d_s, \quad (9)$$

where quark tensor charges appear as the coefficients in front of the corresponding quark EDMs. In these two equations, the heavy flavor contributions are neglected, and isospin symmetry is applied in equation (9). Notably, a phenomenological study in [43] puts experimental constraints on quark EDMs by combining nucleon EDM measurements with tensor charge extractions. With the current projected sensitivity of the neutron/proton EDM experiments and the existing precision of tensor charge extractions (based on the study from [32]), the upper limit on quark EDMs is  $1.27 \times 10^{-24} e \cdot \text{cm}$  for the  $u$  quark, and  $1.17 \times 10^{-24} e \cdot \text{cm}$  for the  $d$  quark, where a 10% uncertainty from the isospin symmetry breaking is included. Both are determined at the scale of  $4 \text{ GeV}^2$ . Future precise measurements of the tensor charge from the SoLID SIDIS program and the nucleon EDMs will reduce the upper limit on quark EDMs by about three orders of magnitude, i.e. to the level of  $10^{-27} e \cdot \text{cm}$  [43]. Based on the result from a dimensional analysis that gives the quark EDM as  $d_q \sim \frac{em_q}{4\pi\Lambda^2}$  [44], we estimate the new physics scale probed by the current quark EDM limit to be about 1 TeV. With the quark EDM limit improved by three orders of magnitude from future experiments, it can probe new physics up to 30–40 TeV [43], beyond the LHC energy.

#### 4. Parity violating deep inelastic scattering

The main observable to be measured by the PVDIS program of SoLID [8] is the Parity-violating (PV) cross section asymmetry, defined as

$$A_{RL} \equiv \frac{\sigma_R - \sigma_L}{\sigma_R + \sigma_L}, \quad (10)$$

where  $\sigma_{R,L}$  are differential cross sections of right- and left-handed incoming electron, respectively. The first PVES experiment, SLAC E122 [45, 46], played a pivotal role in establishing the Standard Model of electroweak physics. During the 6 GeV era of JLab, PVES has provided data on the strangeness content of the nucleon (see e.g. G0 experiment [47, 48]), the excess of the neutron distribution in heavy nuclei and its connection to neutron star physics [49], and determination of the proton weak charge [50, 51] as a test of the SM [52].

Furthermore, through the measurement of  $A_{RL}$  in DIS, a measurement of the effective electron-quark neutral current couplings  $g_{VA}^{eq}$  [53, 54] was completed which improved the precision of SLAC E122 by an order of magnitude.

In the DIS region, the asymmetry can be written as

$$A_{PV} = -\frac{G_F Q^2}{4\sqrt{2}\pi\alpha}[a_1 + a_3 Y], \quad (11)$$

where  $G_F = 1.166 \times 10^{-5} \text{ GeV}^{-2}$  is the Fermi constant,  $\alpha$  is the fine structure constant, and

$$a_1(x) = 2g_A^e \frac{F_1^{\gamma Z}}{F_1^\gamma}, \quad a_3(x) = g_V^e \frac{F_3^{\gamma Z}}{F_1^\gamma}. \quad (12)$$

The structure functions  $F_{1,3}^{\gamma, \gamma Z}$  can be written in the parton model in terms of PDFs  $q_i(x, Q^2)$  and  $\bar{q}_i(x, Q^2)$  of the target:

$$F_1^\gamma(x, Q^2) = \frac{1}{2} \sum Q_{q_i}^2 [q_i(x, Q^2) + \bar{q}_i(x, Q^2)], \quad (13)$$

$$F_1^{\gamma Z}(x, Q^2) = \sum Q_{q_i} g_V^i [q_i(x, Q^2) + \bar{q}_i(x, Q^2)], \quad (14)$$

$$F_3^{\gamma Z}(x, Q^2) = 2 \sum Q_{q_i} g_A^i [q_i(x, Q^2) - \bar{q}_i(x, Q^2)]. \quad (15)$$

Here,  $Q_{q_i}$  denotes the quark's electric charge and the summation is over the quark flavors  $i = u, d, s \dots$ . The  $g_{V,A}^{e,i}$  are the vector and axial coupling of the electron or quark of flavor  $i$ , and in the SM are determined by the weak mixing angle and the electric and weak hypercharge of the particle. The variable  $Y$  is a kinematic factor given approximately by

$$Y = \frac{1 - (1 - y)^2}{1 + (1 - y)^2}. \quad (16)$$

Detailed expressions of  $Y$  that include target-mass effect and the longitudinal structure function  $F_L$  can be found in [54].

Equation (11) shows that by measuring the PVDIS asymmetry on the proton or nuclei, different physics topics can be explored. The PVDIS program of SoLID includes three components: the PVDIS deuteron program is aimed at the precision determination of electroweak parameters and a search for Beyond-the-Standard Model (BSM) physics; the PVDIS proton program that will provide the PDF ratio  $d/u$  in the valence quark region free of nuclear model dependence; and the PVEMC program that will study isospin dependence of the EMC effect by the use of neutron-rich isotopes. With SoLID fully exploring the high luminosity potential of CEBAF, we expect to improve the precision of PVDIS measurement by a factor of ten compared with 6 GeV.

#### 4.1. PVDIS deuteron measurement

**4.1.1. SoLID as a EW/BSM facility.** The SM is a theoretical framework that explains successfully nearly all existing phenomena of particle physics. On the other hand, it is often referred to as an effective theory at the electroweak scale, and believed to be only part of a theory that would ultimately encompass all three (or four) interactions of nature. Given that current evidence of new physics, such as dark matter and neutrino mass, allows many possibilities to extend the SM to higher energy scales, it is imperative that we carry out as many high-precision measurements as possible to test the SM and to shed light on where BSM physics might occur.

The high-intensity beam of CEBAF provides a unique opportunity for SM and BSM study. The reach of experiments that search for BSM physics, if focused on new heavy particles, can be approximately characterized by the product  $s\sqrt{\mathcal{L}}$  where  $\mathcal{L}$  is the luminosity and  $s$  is the center-of-mass energy of the lepton–nucleon scattering process. Even with the EIC coming online in the near future, the BSM reach of fixed-target experiments at JLab is still at least one order of magnitude higher than the EIC if the intensity of CEBAF’s 11 GeV beam is matched by the use of a large acceptance spectrometer, placing SoLID at a unique position to provide an impact on the landscape of EW/BSM physics study for the next decade(s).

**4.1.2. Determination of EW parameters.** To access EW parameters, we measure the PVDIS asymmetry on a deuteron target, for which the SM expression simplifies to:

$$A_{PV,(d)}^{SM} = \frac{3G_F Q^2}{10\sqrt{2}\pi\alpha} [(2g_{AV}^{eu} - g_{AV}^{ed}) + R_V Y (2g_{VA}^{eu} - g_{VA}^{ed})], \quad (17)$$

where  $R_V(x) \equiv (u_V + d_V)/(u^+ + d^+)$  with  $q^+ \equiv q(x) + \bar{q}(x)$  and  $q_V \equiv q(x) - \bar{q}(x)$ . Using the appropriate electric charge and the weak isospin of quarks, they are related to the weak mixing angle  $\theta_W$ . We define the low energy electron-quark effective couplings, given in the SM at the tree level as:

$$g_{AV}^{eu} = 2g_A^e g_V^u = -\frac{1}{2} + \frac{4}{3} \sin^2 \theta_W, \quad (18)$$

$$g_{VA}^{eu} = 2g_V^e g_A^u = -\frac{1}{2} + 2 \sin^2 \theta_W, \quad (19)$$

$$g_{AV}^{ed} = 2g_A^e g_V^d = \frac{1}{2} - \frac{2}{3} \sin^2 \theta_W, \quad (20)$$

$$g_{VA}^{ed} = 2g_V^e g_A^d = \frac{1}{2} - 2 \sin^2 \theta_W. \quad (21)$$

Note that in BSM physics extensions, the couplings may no longer be expressed as products of electron and quark couplings.

Using 120 d of 50  $\mu$ A electron beam with 85% polarization incident on a 40 cm long liquid deuterium target, we can measure the PVDIS asymmetry to sub-percent-level precision within a wide ( $x$ ,  $Q^2$ ) range, see figure 11. The dominant uncertainties will be from experimental systematics including beam polarimetry (0.4%) and  $Q^2$  determination (0.2%), assumed to be fully correlated among all bins, and radiative corrections (0.2%) and event reconstruction (0.2%), assumed to be fully uncorrelated in the present projection study. The treatment of both radiative corrections and event reconstruction as uncorrelated is a simplifying assumption and will be studied in full in the actual data analysis.

Fitting projected  $A_{PV}$  data using the function:

$$A_{PV}^{\text{data}} = A_{PV,(d)}^{SM} \left( 1 + \frac{\beta_{\text{HT}}}{(1-x)^3 Q^2} + \beta_{\text{CSV}} x^2 \right), \quad (22)$$

where  $A_{PV,(d)}^{SM}$  is expressed in terms of  $\sin^2 \theta_W$  and accounting for all correlated and uncorrelated systematic effects, we arrive at the uncertainty projection shown in figure 12. In equation (22), the use of the two  $\beta$  parameters is to account for possible hadronic effects, to be discussed in section 4.2.

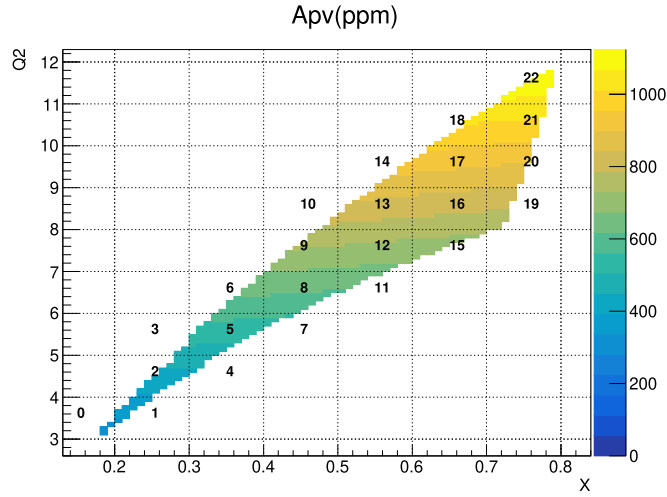


**Figure 11.** Illustration of PVDIS asymmetry on a deuteron target in ppm on the  $(x, Q^2)$  plane. The data are divided into evenly spaced grid with the bin number shown. The expected statistical uncertainty is less than 1% in most of the bins.

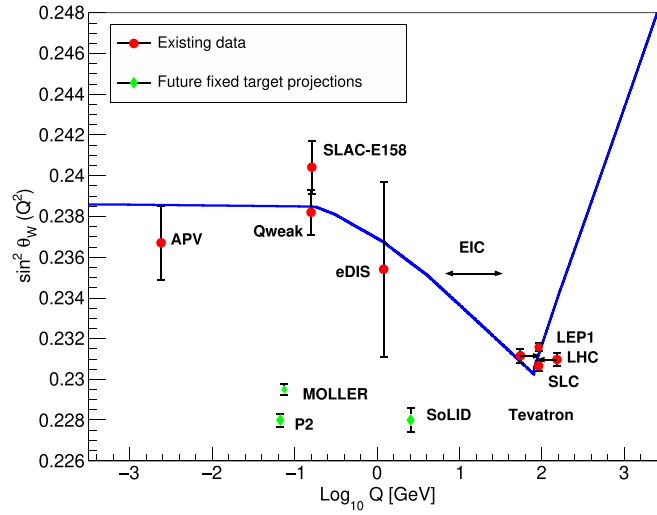


**Figure 12.** Experimental determination of the weak mixing angle  $\sin^2 \theta_W$ . Data points for Tevatron and LHC are shifted horizontally for clarity.

The SoLID deuteron PVDIS measurement, along with the upcoming MOLLER [55] at JLab and the P2 experiment [56] at the MESA facility in Mainz, will provide three new cornerstone measurements of the weak mixing angle  $\sin^2 \theta_W$  in the low to intermediate energy region. Regarding relevant BSM physics, one possible extension is for a dark boson ( $Z_d$ ) that would induce an apparent deviation of  $\sin^2 \theta_W$  from the SM prediction at low  $Q^2$ . In this scenario, a comparison of all three experiments will help to determine the mass of the  $Z_d$ . Here, SoLID PVDIS is unique in that its  $Q^2$  range will help to distinguish between  $Z_d$  of light masses 50 – 200 MeV [57] and those of intermediate masses (10–35) GeV [58]. Another

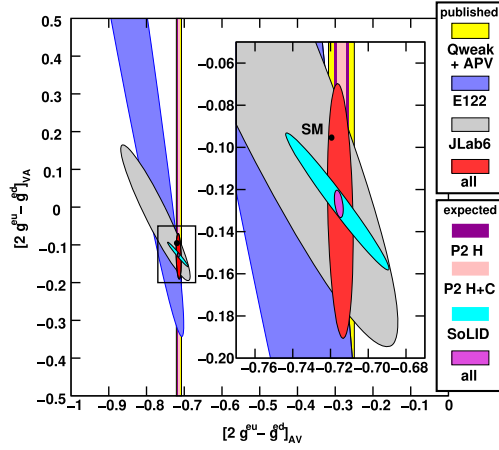


**Figure 13.** Current experimental knowledge of the couplings  $g_{VA}^{eq}$  (vertical axis). The latest world data constraint (red ellipse) is provided by combining the 6 GeV Qweak [51] on  $g_{AV}^{eq}$  (yellow vertical band) and the JLab 6 GeV PVDIS [53, 54] experiments (gray ellipse). The SoLID projected result is shown as the cyan ellipse. Also shown are expected results from P2 (purple and pink vertical bands) and the combined projection using SoLID, P2, and all existing world data (magenta ellipse), centered at the current best-fit values. Adapted from [63], with permission from Springer Nature.

possible extension involves a heavy dark photon [59], whose parameter space can be constrained by PVES, Atomic PV, and the recent results on the  $W$  mass [60, 61].

Furthermore, to fully explore BSM physics, one must study as many individual components of lepton-lepton or lepton-quark interactions as precisely as possible, in addition to the weak mixing angle. The upcoming MOLLER, P2, and the SoLID PVDIS deuteron measurements will provide precision measurements of the low-energy effective couplings  $g_{VA}^{ee}$ ,  $g_{VA}^{eq}$ , and  $g_{AV}^{eq}$ , respectively. For PVDIS, we do so by expressing  $A_{PV,(d)}^{\text{SM}}$  in equation (22) as functions of the electron-quark effective couplings and perform a simultaneous fit of the combinations  $(2g_{AV}^{eu} - g_{AV}^{ed})$  and  $(2g_{VA}^{eu} - g_{VA}^{ed})$ , shown as the cyan-colored ellipse in figure 13. The PVDIS projection can be further combined with that from P2 to provide a global fit, represented by the magenta-colored ellipse. Due to the small value of  $g_{VA}^{eq}$ 's in the SM, they could be particularly sensitive to BSM physics. One model that the  $g_{VA}^{eq}$ 's are sensitive to involves the leptophobic  $Z$ 's [62], corresponding to additional neutral gauge bosons ( $Z'$ ) with negligible couplings to leptons, and thus would cause only sizable axial couplings to quarks while leaving the  $g_{AV}^{eq}$  unaffected.

**4.1.3. BSM reach of PVDIS with SoLID.** The potential of BSM searches can be generally characterized by the mass scale  $\Lambda$ , quantified as modifications of the SM Lagrangian by replacing

$$\frac{G_F}{\sqrt{2}} g_{ij} \rightarrow \frac{G_F}{\sqrt{2}} g_{ij} + \eta_{ij}^q \frac{4\pi}{(\Lambda_{ij}^q)^2}, \quad (23)$$

where  $ij = AV, VA$ . We assume that the new physics is strongly coupled with a coupling  $g$  given by  $g^2 = 4\pi$ , and  $\eta_{ij}^q = \pm 1$  corresponds to cases where the new physics increases (+1, constructive) or decreases (−1, destructive) the couplings. Once combined with the expected results from the P2 experiment [56], the 90% C.L. mass limit that can be reached by the

SoLID PVDIS deuteron measurement is

$$\Lambda_{VA}^{eq} = g \sqrt{\frac{\sqrt{2} \sqrt{5}}{G_F 1.96 \Delta (2g_{VA}^{eu} - g_{VA}^{ed})}} = 17.6 \text{ TeV}, \quad (24)$$

where the  $\sqrt{5}$  represents the ‘best case scenario’ where BSM physics affects maximally the quark flavor combination being measured [64]. Such BSM limits are complementary to those obtained from high-energy facilities. As an example: the LHC Drell-Yan cross section data determine certain combinations of both the parity-violating and parity-conserving electron-quark couplings, defined by the observable measured. As a result, the LHC constraints appear to have a flat direction in the BSM parameter space [65]. In this context, PVDIS observables are sensitive to different combinations of the couplings, resolving the ambiguity in the determination of BSM parameters.

SoLID will undoubtedly push forward the EW/BSM physics study in the low to medium energy regime. On the other hand, a variety of challenges exist. First, one must carry out both electromagnetic and electroweak radiative corrections to high precision. Significant progress has been made on this topic: The event generator *Djangoh* [66], originally developed for HERA cross section analysis, has been adapted to fixed-target experiments and to nuclear targets. Modifications were made such that it can be used to calculate parity violating asymmetries to high precision, immune to the statistical limit of a Monte-Carlo program. While there is still detailed work to be done, we anticipate that the 0.2% uncertainty projected on the radiative corrections can be reached. Such progress will also be useful for similar program at the EIC.

#### 4.2. PVDIS proton measurement and hadronic physics study

In equation (22), the use of the two  $\beta$  parameters is to account for possible hadronic effects:  $\beta_{HT}$  for a higher twist (HT) and  $\beta_{CSV}$  for CSV [67] at the quark level, both expected to have distinct  $x$  and  $Q^2$  dependencies, especially at high  $x$  values. The PVDIS deuteron measurement has the special property that most HT effects cancel in the asymmetry, and thus any sizable HT contribution will indicate the significance of quark-quark correlations [68]. The CSV effect refers to the possibility that the up quark PDF in the proton and down-quark PDF in the neutron are different. Together, these hadronic physics effects may support certain explanations of the apparent inconsistency of the NuTeV experiment [69] with the SM [70, 71].

In addition to the deuteron measurement, PVDIS asymmetries on the proton target will allow us to determine PDF ratio  $d(x)/u(x)$  at high  $x$  based on the dependence of the structure functions in equation (11). The standard determination of the  $d/u$  ratio relies on fully inclusive DIS on a proton target compared to a deuteron target. In the large  $x$  region, nuclear corrections in the deuteron target lead to large uncertainties in the  $d/u$  ratio. However, they can be completely eliminated if the  $d/u$  ratio is obtained from the proton target alone. For a proton target in the parton model and omitting sea quark distributions [63], the PVDIS asymmetry is given by:

$$A_{PV,(p)} = \frac{3G_F Q^2}{2\sqrt{2}\pi\alpha} \frac{\left(2g_{AV}^{eu} - \frac{d}{u}g_{AV}^{ed}\right) + Y\left[2g_{VA}^{eu} - \frac{d}{u}g_{VA}^{ed}\right]}{4 + \frac{d}{u}}, \quad (25)$$

which provides direct access to  $d/u$  without any nuclear physics effects.

In this way, SoLID is complementary to the recent MARATHON experiment at low  $Q^2$  as well as  $W$  production data from Fermilab at high  $Q^2$  [74]. The MARATHON data have been

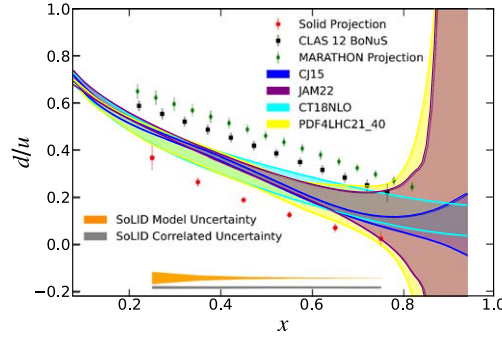


**Figure 14.** Projected results on the PDF ratio  $d/u$  from the PVDIS proton measurement (red points) compared with the current world fits from a number of PDF groups and their uncertainties. The error bars of the SoLID projection indicates the uncertainty in the extracted  $d/u$  from statistical uncertainties, while uncorrelated systematic uncertainties are negligible. The two horizontal shaded bands show the uncertainty in  $d/u$  due to omitting sea quarks in equation (25) (model uncertainty, orange-colored band), and from correlated systematic uncertainties (dark gray band). Projections on MARATHON and CLAS12 BoNuS are from their respective experimental proposals [72, 73].

interpreted in different ways [75–77], highlighting the importance of the PVDIS proton measurement that will provide information both directly on  $d/u$  and on nuclear physics models relevant for future inclusive scattering measurement involving the deuteron or heavier nuclear targets. Using 90 d of 50  $\mu$ A electron beam with 85% polarization incident on a 40 cm long liquid hydrogen target, the projection on  $d/u$  is shown in figure 14.

SoLID in its PVDIS configuration can be used to study more hadronic physics topics. For example, data on PV asymmetry for nucleon resonances will be collected simultaneously with PVDIS running. Resonance  $A_{PV}$  data will help to test how well we model the nucleon, explore quark–hadron duality in the electroweak sector, and help constrain inputs for radiative corrections of PVDIS. Measurements of the beam-normal single-spin asymmetry  $A_n$  provides information on two-photon-exchange physics, see section 7.4.

#### 4.3. Flavor dependence of the EMC effect

Just as PVDIS can be used to study the  $d/u$  ratio in the valence quark region when measured for the proton, it can also be used to study the flavor structure of PDFs if a nuclear target is used. For an isoscalar target with mass number  $A$ , where charge symmetry provides the expectation  $u_A(x) = d_A(x)$ , the PVDIS asymmetry is independent of the EMC effect as long as all PDFs are modified in the same way. In an isoscalar nucleus such as a deuteron or  $^{40}\text{Ca}$ , it can be used to look for charge symmetry violation, although the expectation is that this would yield a small effect (as discussed in section 4.2): While the EMC effect modifies the PDFs in these nuclei, it is assumed that the modification of the up- and down-quarks is identical, and as such, will cancel exactly in the ratio of  $F_1^{\gamma Z}/F_1^{\gamma}$  and  $F_3^{\gamma Z}/F_1^{\gamma}$ , making the asymmetry completely insensitive to the conventional (flavor-independent) EMC effect.

If the EMC effect yields different nuclear modification for the up-quark and down-quark PDFs, this modifies  $A_{PV}$  making it sensitive to the flavor dependence of the EMC effect. In non-isoscalar nuclei, the flavor dependence that arises from the difference in Fermi smearing for protons and neutrons is expected to be extremely small, except for  $x > 0.7$ – $0.8$ , as conventional smearing and binding effects are a small part of the EMC effect [78, 79]. Over the



past decade there have been several indications that the EMC effect may have a significant flavor dependence in non-isoscalar nuclei, as seen in calculations of the EMC effect using different coupling for up- and down-quarks to the QCD scalar and vector potentials [80], and PDF analyzes [81, 82] which explains the tension between neutrino charged-current scattering and DIS plus Drell-Yan data by allowing for a flavor-dependent EMC effect. In addition, a range of models [83] inspired by the observed correlation between the EMC effect and short-range correlations [84, 85] also predict a flavor dependence of the EMC effect associated with the isospin structure of short-distance or high-momentum pairs of nucleons. In all cases, these models, calculations and fits predict an increase in the EMC effect for protons inside of neutron-rich nuclei.

An experiment has been conditionally approved by JLab PAC50 [9] to measure PVDIS on  $^{48}\text{Ca}$ . The experiment, called PVEMC, uses the exact same configuration as the PVDIS measurements on hydrogen and deuterium, except with a  $2.4 \text{ g cm}^{-2}$   $^{48}\text{Ca}$  target. The  $^{48}\text{Ca}$  was chosen to provide a nucleus with a significant EMC effect and a large neutron excess, while avoiding very high- $Z$  material which would yield significantly more radiation for the same target thickness. The kinematic coverage is similar to that shown in figure 11, though the data will be binned only in  $x$  and with a statistical precision at about 1% or less within each  $x$  bin accumulated with 68 d of data taking. The experimental systematic uncertainties are expected to be also similar to the deuteron measurement.

From the measured  $A_{\text{PV}}$ , we can extract the dominant  $a_1$  contribution (equation (11)) which is sensitive to the  $d/u$  ratio of the nuclear structure function. This sensitivity is clear if one evaluates  $a_1$  under the assumption that only light quark distributions  $u_A(x)$  and  $d_A(x)$  contribute and express  $a_1$  as:

$$a_1 \simeq \frac{9}{5} - 4 \sin^2 \theta_W - \frac{12 u_A^+ - d_A^+}{25 u_A^+ + d_A^+} \quad (26)$$

with the convention that  $q^\pm = q(x) \pm \bar{q}(x)$ . This expression is a good approximation at large  $x$ , where the sea quarks do not contribute significantly, and shows that the PVDIS asymmetries are directly sensitive to flavor dependence of the EMC effect that modifies  $u_A^+$  and  $d_A^+$  differently.

Figure 15 shows the projected uncertainties for the proposed measurement, including statistical and systematic uncertainties, as well as the estimated uncertainty on the baseline prediction in the absence of a flavor-dependent EMC effect. The points are shown on the flavor-independent prediction, and the various curves represent projections based on calculations or simple models of the EMC effect, as described in the caption. The projected results give  $7\sigma$  sensitivity to the CBT model prediction [80] and  $>3\sigma$  sensitivity to all but the smallest effect among the models evaluated. Thus, the data will provide a search for a non-zero flavor dependence in the EMC effect, be able to differentiate between ‘large’ and ‘small’ effects and set stringent limits on such a flavor-dependent effect should the results be consistent with a flavor-independent effect.

The presence and size of a flavor-dependent modification of the nuclear PDFs has wide-ranging implications. First, the size of the flavor dependence is sensitive to the underlying physics behind the EMC effect. In addition, observing a flavor-dependent EMC effect would imply that the PDFs used for non-isoscalar nuclei are incorrect, modifying the expectation for high-energy lepton-nucleus scattering such as  $e-A$  or for  $A-A$  collisions. This could be significant for heavy nuclei which have a large neutron excess, as well as for measurements utilizing polarized  $^3\text{He}$  as an effective neutron target.

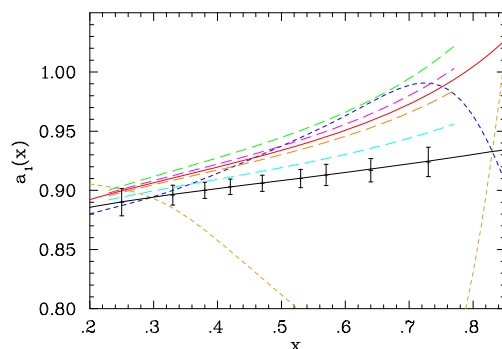


**Figure 15.** Projections for the extracted  $a_1(x)$  for the PVEMC proposal [9] (black points), including statistical, systematic, and normalization (0.4%) uncertainties. The black curve represents the prediction for the flavor-independent EMC effect, the red curve is the CBT model [80], the long-dashed curves represent the predictions from simple scaling models mentioned above [83], and the short-dashed curves represent extreme cases where the EMC effect is caused entirely by up-quark (blue) or down-quark (brown) modification.

## 5. Near-threshold $J/\psi$ production

The proton's fundamental properties, like its electric charge, mass, and spin, are the hallmarks of our knowledge of the visible universe. More than 60 years ago, through a novel experimental investigation of its charge using electron scattering, we learned that the proton is not a point-like particle but has a finite volume with primary constituents. In the following 20 years, these constituents dubbed 'partons' were identified through electron and muon deep inelastic scattering studies as being the quarks and gluons we know today. In tandem, the theory of strong interactions, a non-abelian field theory known as QCD [86–88] was developed and brought our understanding and knowledge of the proton's interior to a new level. In practice, the theory was intractable analytically but could be approximated and tested such as in DIS experiments. Our naive three-valence quark picture providing the total spin  $1/2$  of the proton was challenged, and experimental studies in the last 40 years have described the proton's spin in terms of its partonic structure front and center. Today we know that both constituents quarks gluons and their angular momentum play a role in providing the proton's total spin  $1/2$ . Furthermore, the spin of the proton provided a laboratory to test and better understand QCD with various controlled approximations in corners of its full phase space.

Many studies have focused on the proton electric charge and spin. The proton mass, however, has received less attention. Although the proton's total mass is measured and calculated in QCD with high precision [89, 90], its origin, gravitational density distribution, among its partonic constituents and the trace anomaly are yet to be investigated and fully understood through direct measurements. A few facts are crucial to know why further studies are needed to get a deeper insight into the constituents' role in providing the proton's total mass. First, it is well known that the Higgs mechanism provides for the mass of the quark constituents and breaks chiral symmetry in the QCD Hamiltonian. However, this is only a small fraction of the proton's total mass, about 10%. Second, we also know that scale symmetry is broken in QCD, and this violation is responsible for most of the proton mass. This is reflected by contributions from the gluons' energy, self-interactions, and interactions with the moving quarks.

Recent measurements at JLab [91, 92], motivated by the LHCb charm pentaquarks discovery [93, 94], have given new impetus to using the  $J/\psi$  particle, a small color dipole, not only to search for these pentaquarks but also to probe the gluonic gravitational mass density in the proton and determine the mass radius and scalar radius. These two radii encode information contained in the gluonic gravitational form factors (GFFs) known as  $A_g(k)$  and  $C_g(k)$  form factors, where  $A_g(k)$  is the response to a graviton-like tensor glueball ( $2^{++}$ ) probe and  $C_g(k)$  is a response to a scalar ( $0^{++}$ ) probe. Because the production of the  $J/\psi$  particle at JLab occurs at photon energies near threshold, the region of the measurement is highly non-perturbative. Different theoretical approaches with various approximations have been explored in this non-perturbative region of production to extract these gravitational form factors [95–101]. Recent lattice QCD calculations [102, 103] of these gravitational form factors, albeit at a large pion mass of 450 MeV, will enable comparisons with the various extraction methods of the GFFs.

Close to threshold, the smallness of the electro- and photoproduction cross sections requires a dedicated experiment with a well-designed detector to exploit the full potential of the beam luminosity and capture the full phase space of this process in a measurement of key observables. SoLID provides all the necessary tools to realize the highest statistics exclusive measurements of  $J/\psi$  through both the  $e^+e^-$  and  $\mu^+\mu^-$  channels while cross-checking these two complementary channels and controlling the systematic errors.

### 5.1. The SoLID $J/\psi$ experiment

The detector setup for SoLID- $J/\psi$  [7] is similar to SoLID-SIDIS, except for the unpolarized liquid hydrogen target. The nominal luminosity for SoLID- $J/\psi$  is 50 d at  $10^{37} \text{ cm}^{-2}\text{s}^{-1}$ . In figure 16 we show the kinematic phase space reachable for the electroproduction and photoproduction channels for the nominal luminosity.

The photoproduction channel receives approximately equal contributions from quasi-real electroproduction events and direct photoproduction events due to bremsstrahlung in the extended target. The photoproduction channel maximizes the statistical impact the SoLID- $J/\psi$  experiment can achieve. We measure these events by requiring a coincidence between the  $J/\psi$  decay electron–positron pair and the recoil proton.

To measure the electroproduction events, we measure the scattered electron in coincidence with the  $J/\psi$  decay electron–positron pair. For a subset of events, we also detect the recoil proton for a full exclusive measurement. This redundant measurement is important for understanding the physics and detector backgrounds necessary to precisely determine the absolute cross section.

The projected 1D cross section results for the nominal luminosity is shown in figure 17. The photoproduction and electroproduction channels are truly complementary to each other: the photoproduction channel has superior statistics and  $t$ -reach at higher  $W$ , while electroproduction has superior reach in the region very close to the threshold. The relation between the photon virtuality  $Q^2$  and  $W$  are shown in figure 18. The average  $Q^2$  at threshold is about 1  $\text{GeV}^2$ , dropping as a function of  $W$ . Combining the electroproduction results with the photoproduction results yields a modest but important lever arm in  $Q^2$ .

### 5.2. Gluonic gravitational form factors and SoLID

The  $t$ -dependent differential cross sections measurements that can be achieved by SoLID are shown in figure 19. The process to determine gluonic GFFs from the near-threshold  $J/\psi$  differential cross section is currently under active discussion. One common theme to all proposed approaches [95–101] is the need to precisely measure the  $J/\psi$  differential cross

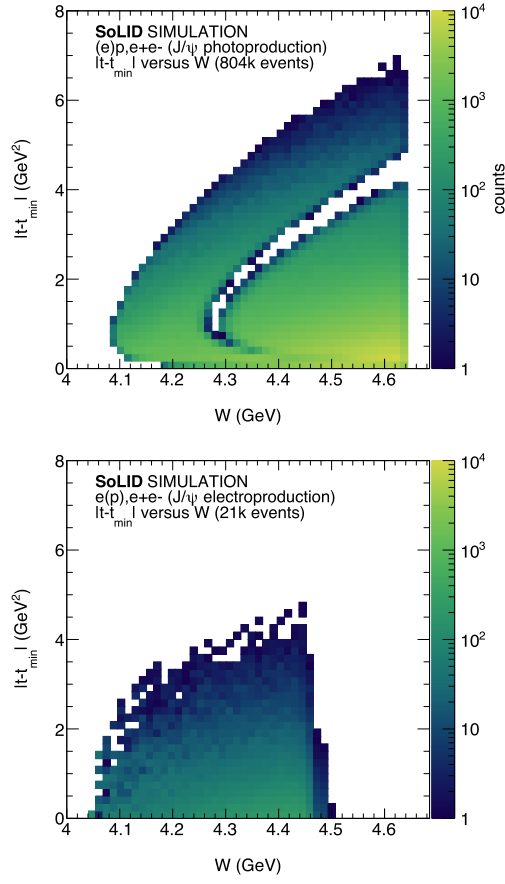


**Figure 16.** Mandelstam variable  $|t - t_{\min}|$  versus the invariant mass of the final state  $W$  for exclusive photo-(top) and electroproduction (bottom) of  $J/\psi$  near threshold. The high statistics of the photoproduction channel allow for a precise measurement of the  $t$ -dependence at larger values of  $t$ , important for constraining gravitational form factors. The electroproduction measurement complements the photoproduction measurement through improved acceptance near threshold.

section at larger values of  $t$  as a function of the photon energy  $E_\gamma$ . A precise determination of the cross section at larger values in  $t$  will help constrain extrapolation uncertainties, while enabling theoretical approaches that depend on a factorization at larger values of  $t$ . This measurement can only be accomplished with SoLID, due to the unique combination of large luminosity and large acceptance for this process.

### 5.3. Other quarkonium production experiments at JLab and EIC

The increased profile of the physics topics that can be studied through near-threshold quarkonium production has spurred many experimental efforts at JLab and is an important component of the EIC scientific program [104]. The first 1D and 2D  $J/\psi$  cross section results near threshold have been published by respectively GlueX and the Hall-C  $J/\psi$ -007 experiment. In the next years, GlueX and CLAS12 will precisely measure the differential  $J/\psi$  cross section at lower values of  $t$ . SoLID- $J/\psi$  will fulfill a unique role within the JLab program for

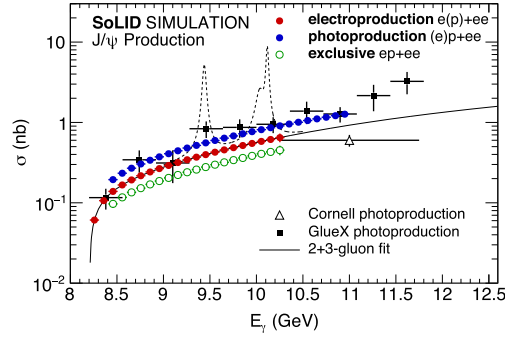


**Figure 17.** Projected 1D  $J/\psi$  cross section results as a function of photon energy  $E_\gamma$  compared with the available world data. The blue disks show the photoproduction results, while the red disks show the electroproduction results and the green circles show the results for a fully exclusive electroproduction measurement. Each of the measurements on this figure has a corresponding high-precision measurement of the  $t$ -dependent differential cross section.

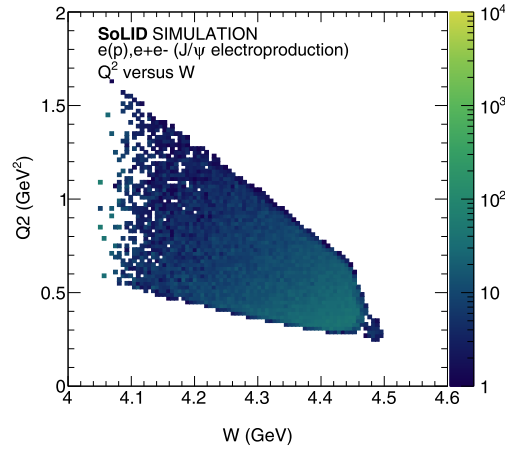


**Figure 18.** Photon virtuality  $Q^2$  versus the invariant mass of the final state  $W$  for exclusive and electroproduction (bottom) of  $J/\psi$  near threshold. At the threshold, there is a modest lever arm in  $Q^2$ , with an average virtuality of about  $1 \text{ GeV}^2$ .

near-threshold  $J/\psi$  production, by precisely measuring the differential cross section at larger values of  $t$ , and by enabling a precise measurement of near-threshold electroproduction. The JLab  $J/\psi$  program is complementary with the near-threshold  $\Upsilon$  program at the EIC.

## 6. GPD program

Generalized parton distributions (GPDs) are a theoretical tool, developed in the late 90s, which offer correlation information between the transverse location and the longitudinal momentum of partons in the nucleon. At leading twist, there are four chiral-odd GPDs ( $H$ ,  $\tilde{H}$ ,  $E$ ,  $\tilde{E}$ ) and four chiral-even GPDs ( $H_T$ ,  $\tilde{H}_T$ ,  $E_T$ ,  $\tilde{E}_T$ ). Each GPD is a function of  $x$ ,  $\xi$  and  $t$ , where

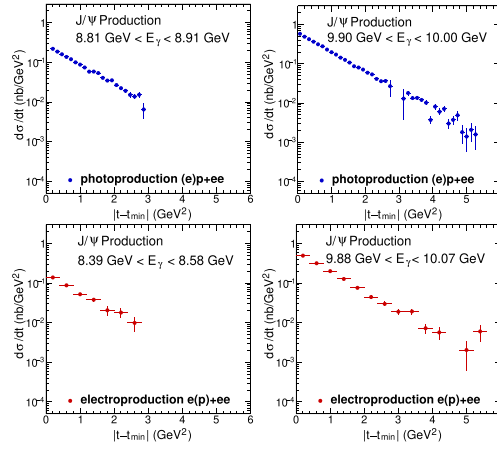


**Figure 19.** Top row: The projected differential cross section for a photoproduction bin at low (left) and high (right) photon energy from figure 17, assuming the nominal luminosity for SoLID- $J/\psi$ . Bottom row: Same for two electroproduction bins. Precise measurements of these  $t$ -dependence over the full near-threshold phase space will hold the key to constrain the GFFs.

$x$  denotes the average light-cone momentum fraction of the quark,  $\xi \approx x_B/(2 - x_B)$  is the skewness representing the longitudinal momentum fraction transferred to the nucleon, and  $t$  represents the total square momentum transferred to the nucleon. GPDs also depend on  $Q^2$ , which is usually dropped out from the expressions since the  $Q^2$ -variation follows the QCD evolution equations. GPDs provide a link between electromagnetic form factors and parton distributions [105–107] and can further access the contribution of the OAM of quarks (and gluons) to the nucleon spin through the Ji’s sum rule [108],

$$\begin{aligned} J^q &= \frac{1}{2} \Delta \Sigma^q + L^q \\ &= \frac{1}{2} \int_{-1}^{+1} dx \, x [H^q(x, \xi, 0) + E^q(x, \xi, 0)], \end{aligned} \quad (27)$$

where  $\Delta \Sigma^q$  is the quark spin contribution that has been measured in polarized deep inelastic scattering, and  $L^q$  is the quark OAM contribution to the nucleon spin. Note that the sum rule also applies to the gluon GPDs. Hence, Ji’s sum rule provides an experimental way to decompose the nucleon spin in terms of the contributions from the spin polarization and OAM of quarks and gluons.

### 6.1. Deep exclusive meson production

A special kinematic regime is probed in DEMP reactions, where the initial hadron emits a quark-antiquark or gluon pair. This has no counterpart in the usual parton distributions and carries information about  $q\bar{q}$  and  $gg$ -components in the hadron wavefunction. Because quark helicity is conserved in the hard scattering regime, the produced meson acts as a helicity filter [109]. In particular, leading order QCD predicts that vector meson production is sensitive only to the unpolarized GPDs,  $H$  and  $E$ , whereas pseudoscalar meson production is sensitive only to the polarized GPDs,  $\tilde{H}$  and  $\tilde{E}$ . In contrast, DVCS depends at the same time on both the polarized ( $\tilde{H}$  and  $\tilde{E}$ ) and the unpolarized ( $H$  and  $E$ ) GPDs. Thus, DEMP reactions provide a tool to disentangle the different GPDs from experimental data [109].

The  $\tilde{E}$  is particularly poorly known [110]. It is related to the pseudoscalar nucleon form factor  $G_P(t)$ , which is itself highly uncertain because it is negligible at the momentum transfer of nucleon  $\beta$ -decay.  $\tilde{E}$  is believed to contain an important pion pole contribution, and hence is optimally studied in DEMP.  $\tilde{E}$  cannot be related to any already known parton distribution, and so experimental information about it can provide new nucleon structure information unlikely to be available from any other source.

Frankfurt *et al* [111] identified the single spin asymmetry for exclusive  $\pi^\pm$  production from a transversely polarized nucleon target as the most sensitive observable to probe the spin-flip  $\tilde{E}$ . The experimental access to  $\tilde{E}$  is through the azimuthal variation of the emitted pions, where the relevant angles are  $\phi$  between the scattering and reaction planes, and  $\phi_s$  between the target polarization and the scattering plane. The  $\sin(\phi - \phi_s)$  asymmetry, where  $(\phi - \phi_s)$  is the angle between the target polarization vector and the reaction plane, is related to the parton-helicity-conserving part of the scattering process and is sensitive to the interference between  $\tilde{H}$  and  $\tilde{E}$  [111, 112]. The asymmetry vanishes if  $\tilde{E}$  is zero. If  $\tilde{E}$  is not zero, the asymmetry will display a  $\sin(\phi - \phi_s)$  dependence. [111, 113] note that ‘precocious scaling’ is likely to set in at moderate  $Q^2 \sim 2 - 4 \text{ GeV}^2$  for this observable, as opposed to the absolute cross section, where scaling is not expected until  $Q^2 > 10 \text{ GeV}^2$ .

SoLID, in conjunction with a polarized  $^3\text{He}$  target, can be used to probe  $\tilde{E}$ . Since polarized  $^3\text{He}$  is an excellent proxy for a polarized neutron, the reaction of interest is essentially  $\vec{n}(e, e'\pi^-)p$  (after nuclear corrections are applied). The only previous data are from HERMES [114], for average values  $\langle x_B \rangle = 0.13$ ,  $\langle Q^2 \rangle = 2.38 \text{ GeV}^2$ . Although the observed  $\sin(\phi - \phi_s)$  asymmetry moment is small, the HERMES data are consistent with GPD models based on the dominance of  $\tilde{E}$  over  $\tilde{H}$  at low  $-t = -(q - p_\pi)^2$  [115]. An improved measurement of the  $\sin(\phi - \phi_s)$  modulation of the transverse target spin asymmetry, is clearly a high priority. In comparison to HERMES, SoLID will probe higher  $Q^2$  and  $x_B$ , with much smaller statistical errors over a wider range of  $t$ . Thus, the measurements should be more readily interpretable than those from HERMES, providing the first clear experimental signature of  $\tilde{E}$ .

In the DEMP reaction on a neutron, all three charged particles in the final state,  $e^-$ ,  $\pi^-$  and  $p$ , can be cleanly measured by SoLID. Hence, contamination from other reactions, including DEMP from the other two protons in  $^3\text{He}$ , can be greatly eliminated. The dominant background of the DEMP measurement comes from the SIDIS reactions of electron scattering on the neutron and two protons in  $^3\text{He}$ . Further reduction in the background can be accomplished by reconstructing the missing momentum and missing mass of the recoil protons, via  $\vec{p}_{\text{miss}} = \vec{q} - \vec{p}_\pi$ ,  $M_{\text{miss}} = \sqrt{(\nu - E_\pi)^2 - (\vec{q} - \vec{p}_\pi)^2}$ . After applying a missing momentum cut to exclude events for which  $p_{\text{miss}} > 1.2 \text{ GeV}/c$ , the SIDIS background is largely suppressed.

Figure 20 shows E12-10-006B [11] projections for the two most important transverse single-spin asymmetry moments. The  $\sin(\phi - \phi_s)$  moment (left) provides access to  $\tilde{E}$  and is the primary motivation of the measurement. There is growing theoretical interest in the  $\sin(\phi_s)$  moment (right), as it provides access to the higher-twist transversity GPD  $H_T$ . The projected data points assume detection of triple-coincidence  $^3\text{He}(e, e'\pi^-)pp$  events, after application of the  $p_{\text{miss}}$  cut. All scattering, energy loss, and detector resolution are included. Fermi momentum has been turned off in the event generator, similar to where the recoil proton resolution is good enough to correct for Fermi momentum effects on an event-by-event basis. The agreement between the input and output fit values is very good, validating the unbinned maximum likelihood analysis procedure.

The high luminosity and full azimuthal coverage capabilities of SoLID make it well-suited for this measurement. It is the only feasible manner to access to wide  $t$  range needed to fully



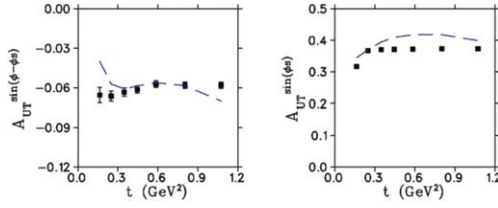


**Figure 20.** Projected uncertainties for  $A_{UT}^{\sin(\phi-\phi_s)}$  and  $A_{UT}^{\sin(\phi_s)}$  in the  $\vec{n}(e, e'\pi^-)p$  reaction from a transversely polarized  $^3\text{He}$  target and SoLID. The dashed curve represents the input asymmetry into the simulation, and the data points represent the extracted asymmetry moment values from an unbinned maximum likelihood (UML) analysis of simulated SoLID data.

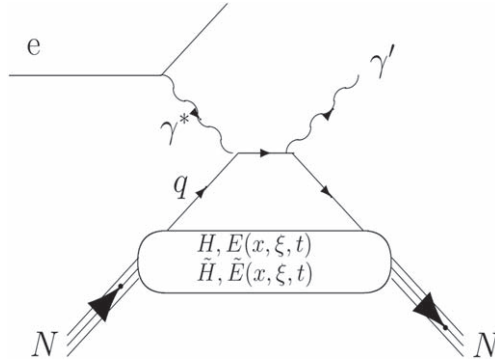


**Figure 21.** DVCS process in the  $e + N \rightarrow eN\gamma$  reaction. The cross section is composed of the amplitudes of DVCS and Bethe–Heitler processes as well as their interference.

exploit the transverse target asymmetry information. The projected SoLID data are expected to be a considerable advance over the HERMES data in terms of kinematic coverage and statistical precision. The SoLID measurement is also important preparatory work for studies of the same asymmetries at the EIC, utilizing a transversely polarized proton or  $^3\text{He}$  beam.

### 6.2. Deeply virtual Compton scattering with polarized targets

Deeply Virtual Compton Scattering (DVCS) is the golden channel to experimentally study GPDs [116, 117]. In electron scattering off nucleons with sufficiently large momentum transfer, a highly virtual photon scatters from a quark and excites the nucleon, which returns to its initial nucleon state by emitting a real photon so the nucleon remains intact. In this process depicted in figure 21, one measures the hard exclusive photons produced in the Bethe–Heitler (BH) and the DVCS processes, as well as their interference, i.e.  $\sigma_{e+N \rightarrow eN\gamma} \propto |\mathcal{T}_{\text{DVCS}}|^2 + |\mathcal{T}_{\text{BH}}|^2 + \mathcal{I}$ , where the DVCS term and the interference term ( $\mathcal{I} = \mathcal{T}_{\text{DVCS}}^* \mathcal{T}_{\text{BH}} + \mathcal{T}_{\text{BH}}^* \mathcal{T}_{\text{DVCS}}$ ) contain the information about the GPDs with the convolution integral, called Compton Form Factors (CFF).

Several DVCS experiments with proton targets have been carried out in Halls A and B of JLab with 6 GeV electron beam [118–121] as well as the HERMES experiment [122–129]. With the 12 GeV upgrade, several experiments in Halls A and B have been approved to measure the beam-spin asymmetry and target-spin asymmetry with a longitudinally polarized proton target [130, 131]. The DVCS measurement on neutrons is more difficult, mainly due to

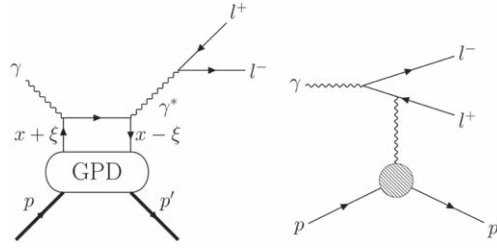


**Figure 22.** Left: handbag diagram of the TCS process. Right: diagram of the BH process.

lower production yields, smaller asymmetries, and bigger demands on the experimental techniques compared with the proton-DVCS case. The first neutron-DVCS measurement [132] was performed in the E03-106 experiment in Hall A with polarized beam on a deuterium target. This pioneering work established the importance of the neutron-DVCS measurement, but was limited to a narrow phase space. An approved CLAS12 experiment [133], aims to measure the beam-spin asymmetry with an unpolarized neutron target.

To allow for a full flavor decomposition to extract the GPDs of individual quarks, it is desired to collect precise neutron data over a more complete phase space and with more experimental observables. It is especially important to do measurements with a transversely polarized target, which is essential to access the poorly known GPD  $E$ . SoLID will enable the first measurement of DVCS on transversely polarized neutrons with 11 GeV longitudinally polarized electron beam, where the single-spin asymmetry ( $A_{UT}$ ) and the double-spin asymmetry ( $A_{LT}$ ) provide great sensitivities to decouple different CFFs in the neutron-DVCS reaction. A run-group measurement, in parallel with the already approved SIDIS experiment (E12-10-006), is under exploration. In combination with the DVCS measurement using polarized proton targets running parasitically with the approved SIDIS experiment (E12-11-108), one can perform flavor decomposition to isolate the CFFs of  $u$  and  $d$  quarks. Possible detector upgrades, including a better energy resolution EM calorimeter or a recoil detector, will enable clean identification of the DVCS events and unlock the full power of the SoLID GPD program.

### 6.3. Timelike Compton scattering

The most widely studied DVCS measurement is the electroproduction of a real spacelike photon on a nucleon. Correspondingly, TCS, is the photoproduction of a virtual timelike photon ( $Q'^2 > 0$ ) on a nucleon, where the final state virtual photon immediately decays into a lepton pair, as shown in equation (28) and the left panel of figure 22 [134]. Like DVCS, TCS is also a direct process to access nucleon GPDs and can provide valuable information for GPD extraction. The study of both processes provides an upmost important test about the universality of GPDs and the QCD factorization approach.

$$\gamma + p \rightarrow \gamma^* + p' \rightarrow l^- + l^+ + p' \quad (28)$$

TCS is not the only physical process that can be observed in the exclusive photoproduction of lepton pairs, many resonance states decay into lepton pairs as well. In the resonance-free region, the dominant background process with the same final state is the purely electromagnetic BH reaction shown in the right panel of figure 22. Again like DVCS, the TCS and

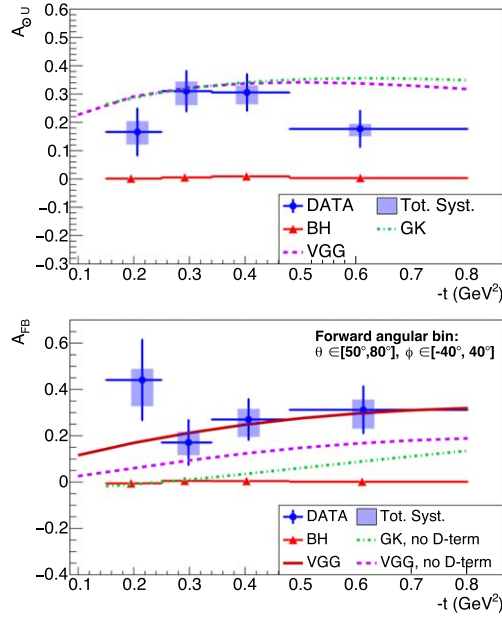


**Figure 23.** The photon polarization asymmetry  $A_{\odot U}$  (top) and forward–backward (bottom) asymmetries as a function of  $-t$  at the averaged kinematic point  $E_\gamma = 7.29 \pm 1.55$  GeV;  $M = 1.80 \pm 0.26$  GeV [134]. The errors on the averaged kinematic point are the standard deviations of the corresponding distributions of events. The data points are represented in blue with statistical vertical error bars. The horizontal bars represent the bin widths. The shaded error bars show the total systematic uncertainty. The red triangles show the asymmetry computed for simulated BH events. The dashed and dashed-dotted lines are the predictions of the VGG and GK models respectively. The solid line shows the model predictions of the VGG model with D-term.

BH amplitudes interfere. Even though the BH cross section is significantly larger than the TCS cross section, we can take advantage of this interference to study TCS.

The JLab-12 GeV upgrade opens the door to access the TCS production in the resonance-free region. The first TCS measurement on proton using the CLAS12 detector was recently published [134] and the selection of results are shown in figure 23. The photon circular polarization and forward–backward asymmetries were measured to be nonzero, providing strong evidence for the contribution of the quark-level mechanisms parametrized by GPDs to this reaction. The comparison of the measured polarization asymmetry with DVCS-data-constrained GPD model predictions for the imaginary and real parts of  $H$  points toward the interpretation of GPDs as universal functions. This is a great achievement, even with limited statistics. It is clear that more measurements are needed to expand the study of TCS.

Experiment E12-12-006A [12] will study the TCS reaction via exclusive  $e^+e^-p$  production, using the SoLID detector with an 11 GeV polarized electron beam and a 15 cm LH<sub>2</sub> target. The experimental observables include the circularly polarized photon asymmetry and the forward–backward asymmetry just like CLAS12, but it can also study the moments of the weighted cross section with more available data. The kinematics can cover a wide range of squared four-momentum transfer ( $0.1 < -t < 0.7$  GeV<sup>2</sup>), outgoing photon virtuality ( $2.25 < Q'^2 < 9$  GeV<sup>2</sup>) and skewness ( $0.1 < \xi < 0.4$ ) with  $\xi = Q'^2 / ((s - m_p^2) - Q'^2)$  where  $s$  is the center-of-mass energy and  $m_p$  is the proton mass. As a run group experiment with the

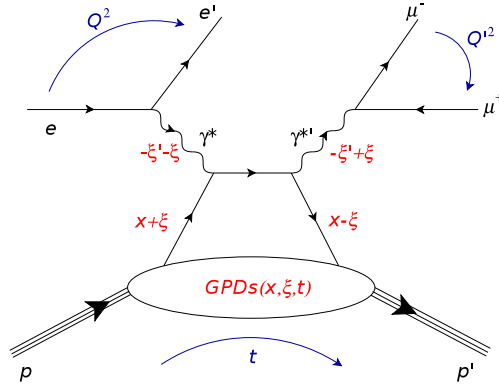


**Figure 24.** Schematic of the direct term of the DDVCS amplitude with a di-muon final state. The full amplitude contains also the crossed term, where the final time-like photon is emitted from the initial quark.  $Q^2 = -q^2$  is the virtuality of the space-like initial photon, and  $Q'^2 = q'^2$  is the virtuality of the final time-like photon.

SoLID J/ $\psi$  program E12-12-006, the two measurements would benefit each other on the normalization and systematic studies.

SoLID TCS is the perfect next stage experiment after the CLAS12 TCS measurement. It will provide an essential cross-check by using a different large acceptance detector to measure the same process. This is a safe approach, since TCS is still a new tool for GPD studies. The high luminosity  $10^{37} \text{ cm}^{-2} \cdot \text{s}^{-1}$  of SoLID is 2 orders magnitude larger than CLAS12, making it possible to perform a mapping of the  $t$ , photon virtuality and skewness dependences at the same time. This is essential for understanding factorization, higher-twist effects, and NLO corrections. The experiment will collect unprecedented amount of high-quality data. It will push the TCS study to a precision era, and together with DVCS, carry out global analyzes to extract GPDs from the data.

#### 6.4. Double deeply virtual Compton scattering (DDVCS)

The dynamical properties of the nucleon that are expressed by the energy-momentum tensor [108] involve integrals of GPDs over the average momentum fraction of partons at fixed skewness. Similarly, the tomography of the nucleon [135] involves integrals of GPDs over the transverse momentum transfer in the zero-skewness limit. Thus, it is of prime importance to obtain a separate knowledge of the  $x$ - and  $\xi$ -dependences of GPDs. Differently from the DVCS and TCS processes, which access GPDs along the line  $x = \pm \xi$ , the DDVCS process [136, 137], where the initial and final photons are virtual, is the only known process allowing one to investigate independently the  $(x, \xi)$ -dependence of GPDs, i.e. at  $x \neq \xi$  (see figure 25).

At leading twist and leading  $\alpha_s$ -order, the DDVCS process corresponds to the absorption of a space-like photon by a parton of the nucleon, followed by the emission from the same parton of a time-like photon decaying into a  $\ell\bar{\ell}$ -pair, see figure 24. The scaling variables attached to this process are defined as

$$\xi' = \frac{Q^2 - Q'^2 + t/2}{2Q^2/x_B - Q^2 - Q'^2 + t} \quad (29)$$

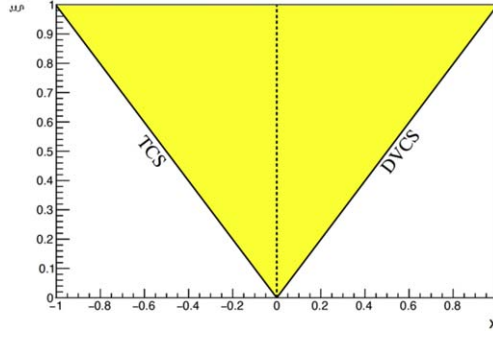


**Figure 25.** Singlet GPD  $F_+(x, \xi, 0)$  coverage of the physics phase-space of the imaginary part of the CFFs: the yellow area represents the DDVCS reach, bounded on the one side by the TCS, and on the other side by DVCS lines. The  $x$ -axis corresponds to the PDFs (parton distribution functions) domain measured in inclusive Deep Inelastic Scattering.

$$\xi = \frac{Q^2 + Q'^2}{2Q^2/x_B - Q^2 - Q'^2 + t}, \quad (30)$$

representing the Bjorken generalized variable ( $\xi'$ ) and the skewness ( $\xi$ ). When the final photon becomes real, the DDVCS process turns into DVCS, which corresponds to the restriction  $\xi' = \xi$  in the Bjorken limit. When instead the initial photon becomes real, DDVCS turns into the TCS process, which corresponds to the restriction  $\xi' = -\xi$  in the Bjorken limit. In these respects, the DDVCS process is a generalization of the DVCS and TCS processes.

The DDVCS reaction amplitude is proportional to a combination of the Compton Form Factors (CFFs)  $\mathcal{F}$  (with  $\mathcal{F} \equiv \{\mathcal{H}, \mathcal{E}, \tilde{\mathcal{H}}, \tilde{\mathcal{E}}\}$ ) defined from the GPDs  $F$  (with  $F \equiv \{H, E, \tilde{H}, \tilde{E}\}$ ) as

$$\mathcal{F}(\xi', \xi, t) = \mathcal{P} \int_{-1}^1 F_+(x, \xi, t) \left[ \frac{1}{x - \xi'} \pm \frac{1}{x + \xi'} \right] dx - i\pi F_+(\xi', \xi, t), \quad (31)$$

where  $\mathcal{P}$  denotes the Cauchy's principal value integral, and

$$F_+(x, \xi, t) = \sum_q \left( \frac{e_q}{e} \right)^2 [F^q(x, \xi, t) \mp F^q(-x, \xi, t)] \quad (32)$$

is the singlet GPD combination for the quark flavor  $q$ , where the upper sign holds for vector GPDs ( $H^q, E^q$ ) and the lower sign for axial vector GPDs ( $\tilde{H}^q, \tilde{E}^q$ ). In comparison to DVCS and TCS, the imaginary part of the DDVCS CFFs accesses the GPDs at  $x = \pm \xi' \neq \xi$ , and the real part of the DDVCS CFFs involves a convolution with different parton propagators. Varying the virtuality of both incoming and outgoing photons changes the scaling variables  $\xi'$  and  $\xi$ , and maps out the GPDs as function of its three arguments independently. From equations (29)–(30), one obtains

$$\xi' = \xi \frac{Q^2 - Q'^2 + t/2}{Q^2 + Q'^2}, \quad (33)$$

indicating that  $\xi'$ , and thus the imaginary parts of the CFFs  $\{\mathcal{H}, \mathcal{E}\}$ , changes sign around  $Q^2 = Q'^2$ . This represents a strong testing ground of the universality of the GPD formalism [138].

Similarly to DVCS, the imaginary part of the CFFs can be accessed by comparing experimental cross sections measured with polarized electron or positron beams of opposite

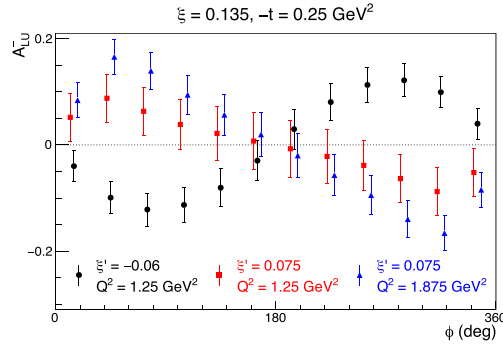


**Figure 26.** Projections of selected DDVCS beam-spin asymmetry measurements with SoLID, assuming 50 d of data taking on a liquid hydrogen target and a luminosity of  $1.2 \times 10^{37} \text{ cm}^{-2} \cdot \text{s}^{-1}$  [141].

helicities, and the real part of the CFFs is best measured by comparing experimental cross sections measured with unpolarized electron and positron beams [139]. In order to achieve these measurements, the SoLID spectrometer is to be completed with specific devices dedicated for muon detection [140]. The Large Angle Muon Detector takes advantage of the material of the large angle electromagnetic calorimeter and the iron flux return to serve as shielding, and two layers of GEMs at the outer radius of the downstream endcap ensure the detection of particles. The Forward Angle Muon Detector, placed after the downstream endcap, consists of three layers of iron slabs instrumented with GEMs. This configuration provides a significant coverage of the DDVCS muons and allows the efficient investigation of the  $(\xi, \xi')$  space for  $Q^2 \leq 3.5 \text{ GeV}^2$  and  $-t < 1 \text{ GeV}^2$ . An unprecedented quantity of data will be collected and can be used to measure cross section and beam-spin asymmetry (BSA) observables of the DDVCS process. The experiment would operate over a period of 50 d with a 15 cm long unpolarized liquid hydrogen target and a  $3 \mu\text{A}$  beam intensity. Selected BSA projections are shown in figure 26. Particularly, it is worth noting that the quality of expected data would permit observation of the predicted sign change of the imaginary part of the CFFs, supporting GPD universality.

Both TCS and DDVCS measurements require detection of dilepton decay of virtual photons with high luminosity and large acceptance. The SoLID spectrometer uniquely meets such a demand. The SoLID TCS and DDVCS programs were featured in the 1st ‘International Workshop on the Nucleon and Nuclear Structure through dilepton Production’ at ECT\* in Trento, Italy in October 2016 and included in the resulting whitepaper [138].

## 7. Other physics topics

The multi-purpose feature of SoLID will allow many other physics topics to be studied, either as rungroup or stand-alone experiments. These physics topics are summarized in this section.

### 7.1. Inclusive transverse spin structure functions

The transverse polarized structure function  $g_2(x, Q^2)$  probes transversely and also longitudinally polarized parton distributions inside the nucleon. It carries the information of quark–gluon interactions inside the nucleon. By neglecting quark masses,  $g_2(x, Q^2)$  can be decoded by a leading twist–2 term and a higher twist term as follows:

$$g_2(x, Q^2) = g_2^{WW}(x, Q^2) + \bar{g}_2(x, Q^2), \quad (34)$$

where twist-2 term  $g_2^{WW}$  was derived by Wandzura and Wilczek [142] and it only depends on well-measured  $g_1$  [143, 144].

The matrix element  $d_2$  is the  $x^2$  moment of  $\bar{g}_2(x, Q^2)$ . This quantity measures deviations of  $g_2(x, Q^2)$  from the twist-2 term  $g_2^{WW}$ . At large  $Q^2$ , where the operator product expansion (OPE) [145] becomes valid, one can access the twist-3 effects of quark–gluon correlations via the third moment of a linear combination of  $g_1(x, Q^2)$  and  $g_2(x, Q^2)$ , presented as

$$\begin{aligned} d_2(Q^2) &= 3 \int_0^1 x^2 [g_2(x, Q^2) - g_2^{WW}(x, Q^2)] dx \\ &= \int_0^1 x^2 [2g_1(x, Q^2) + 3g_2(x, Q^2)] dx. \end{aligned} \quad (35)$$

Due to the  $x^2$ -weighting,  $d_2(Q^2)$  is particularly sensitive to the large- $x$  behavior of  $\bar{g}_2$  and provides us a clean way to access twist-3 contribution.

A precision measurement of neutron spin structure function  $g_2(x, Q^2)$ , running in parallel with this experiment and experiment E12-11-007 [5], has been approved as a run group proposal [146] by PAC48. High statistics data will be collected within a large kinematic coverage of Bjorken scaling  $x > 0.1$  and four-momentum transfer  $1.5 < Q^2 < 10 \text{ GeV}^2$  from inclusive scatterings of longitudinally polarized electrons off transversely and longitudinally polarized  $^3\text{He}$  targets, at incident beam energies of 11 and 8.8 GeV. In addition to mapping out the  $x$  and  $Q^2$  evolution of  $g_2$ , the moment  $d_2(Q^2)$ , which is connected to the quark–gluon correlations within the nucleon, will be extracted with  $1.5 < Q^2 < 6.5 \text{ GeV}^2$ .  $d_2(Q^2)$  is one of the cleanest observables that can be used to test the theoretical calculations from lattice QCD and various nucleon structure models.

## 7.2. SIDIS with Kaon production

While the JLab TMD program mostly focuses on measuring the pion production in SIDIS, the kaon production data are crucial to successfully decouple all light quark flavors. There are only limited kaon-SIDIS data from HERMES [147], COMPASS [148], and JLab Hall A collaborations [149], all of which are with poor precision and narrow kinematic coverage. In the run-group proposal [29], we will perform an offline analysis to extract the kaon-SIDIS events out from all the already approved SoLID pion-SIDIS measurements. The kaon events will be identified using the time-of-flight (TOF) information from the MRPC. A 20 ps time resolution of a new generation MRPC, which has been achieved with cosmic ray test by several groups [150, 151], should be able to perform  $\pi^\pm/K^\pm$  separation up to a high hadron momentum (e.g.  $P_h < 7.0 \text{ GeV c}^{-1}$ ), while the veto-signal from heavy gas Čerenkov detector can also effectively isolate  $K^\pm$  from  $\pi^\pm$ .

Thanks to the high intensity and large acceptance features of the SoLID detector system, the new measurement will generate a large set of kaon data with great precision and a wide kinematic coverage in multiple dimensions as shown in figure 27. The combined analysis of both the pion and kaon SIDIS-data from both proton and neutron ( $^3\text{He}$ ) targets on SoLID will allow us to systematically separate contributions from all light quarks, especially to isolate the sea-quark contributions. The systematic uncertainties can also be largely reduced since the pion and kaon SIDIS events are measured all together. Model estimation shows that at the SoLID kinematics about 20% of the kaon SIDIS events come from the current fragmentation region where the TMD factorization can be applied. The high-quality kaon data from SoLID are crucial for the validation of the model calculation. Our new measurement will provide high-quality data for the continuous theoretical development of the TMD physics, and more



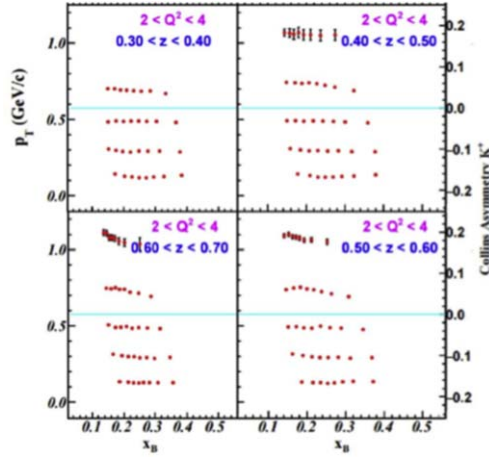


**Figure 27.** One  $Q^2$  bin of the 4D ( $Q^2$ ,  $z$ ,  $p_T$ ,  $x_B$ ) binning projection and statistical uncertainties of the Collins asymmetry ( $A_{UT}^{\sin(\phi+\phi_S)}$ ) in  $\vec{n}(e, e'K^+)X$  with transversely polarized  $^3\text{He}$ . The sizes of the uncertainties are indicated by the Y-axis on the right. See the original proposal for all projection results.

importantly, provide strong guidance to future measurements on EIC, which will fully study the TMD of sea-quarks and gluons in a wider kinematic coverage and provide a more complete image of nucleon structures.

### 7.3. SIDIS with Di-hadron production

Di-hadron SIDIS is an important part of the 12 GeV JLab physics program. Di-hadron single target spin asymmetry provided a wide range of insights into nucleon structure and hadronization. It is one of the easy channels to access the leading-twist PDF  $h_1(x)$ , the so-called transversity distribution function. The combination of the proton and neutron measurements on the transversity distribution function will also allow to operate a flavor separation.

In the process of  $\ell(l) + N(P) \rightarrow \ell(l') + H_1(P_1) + H_2(P_2) + X$ , the transversity distribution function  $h_1(x)$  is combined with a chiral-odd Di-hadron fragmentation function (*DiFF*), denoted as  $H_1^{\tilde{q}q}$ , which describes the correlation between the transverse polarization of the fragmenting quark with flavor  $q$  and the azimuthal orientation of the plane containing the momenta of the detected hadron pair. *DiFF* can be extracted from electron–positron annihilation where two back-to-back jets are produced and a pair of hadrons are detected in each jet. They also appear in the observable describing the semi-inclusive production of two hadrons in deep inelastic scattering of leptons off nucleons or in hadron–hadron collisions. The *DiFFs* also play a role in extending the knowledge of the nucleon collinear picture beyond the leading twist. Contrary to the Collins mechanism, this effect survives after integration over quark transverse momenta and can be analyzed in a collinear factorization framework. Thus this analysis will be much simpler compared to the traditional analysis of single-hadron fragmentation.

Since the di-hadron proposal [28] was accepted in 2014, research has been continued on improving *DiFF* [152, 153]. The first extraction of transversity from a global analysis of electron–proton and proton–proton data was published in 2018 by Radici *et al* [154]. A measurement beam-spin asymmetry of di-hadron has also been published by the CLAS

collaboration [155], which leads to the extraction of the nucleon twist-3 parton distribution function  $e(x)$  [156]. Recent measurements at CLAS12 showed the first empirical evidence of nonzero  $G_1^\perp$ , the parton helicity-dependent *DiFF* encoding spin-momentum correlations in hadronization [157]. All these researches bring more and more attention to the di-hadron beam-spin asymmetries in our field.

#### 7.4. Beam-normal and target-normal SSAs

Our understanding and description of the internal structure of both nuclei and nucleons have seen a steady improvement over the past several decades. These improvements are sometimes brought on by inconsistent or unexplained experimental results, revealing limitations of our underlying assumptions. One such example is that of the discrepancy in the extraction of  $G_E^p/G_M^p$ , the ratio of the proton form factors of elastic scattering from either Rosenbluth or polarization transfer measurements at large  $Q^2$ , see e.g. [158] and references therein. At present, this discrepancy is attributed to TPE and the size of the discrepancy is used to quantify TPE [159]. Conversely, a reliable quantification of the TPE effects is needed to interpret electron scattering data in order to fully understand the structure of the nucleon.

One way that TPE effects have been investigated is through a comparison of electron and positron elastic scattering off the proton, i.e. elastic lepton-charge asymmetry. Such measurements have been made at the VEPP-3 Storage Ring [160], using CLAS [161] at JLab, and by the OLYMPUS experiment at DESY [162]. Studies of TPE also form part of the main thrust of a potential positron program at JLab [163]. However, a precision comparison between electron and positron scattering has its own challenges with one of the main systematic uncertainties being the relative luminosity control between the two beams.

An alternate method to study TPE is through measurements of single spin asymmetries (SSA) where either the lepton (incoming or outgoing) or the target spin is polarized normal to the scattering plane, i.e. polarized along  $\vec{k} \times \vec{k}'$  with  $\vec{k}$  and  $\vec{k}'$  the incoming and scattered electron's momentum, respectively. Experimentally, the most accessible would be the BNSSA or the target-normal SSA (TNSSA). At the Born level, in which a single photon is exchanged, both asymmetries are forbidden due to time-reversal invariance as well as parity conservation [164]. Going beyond the Born approximation, they are no longer restricted and can provide direct access and insight into the imaginary part of the TPE amplitude.

The initial theoretical predictions of both the TNSSA and BNSSA described the interaction in which the two photons couple to the same quark [165], and later, for the TNSSA, one in which the two photons couple to different quarks [166]. Finally, a complete partonic description of the TNSSA now exists [167], in which all contributions have been taken into account.

Experimentally, the TNSSA has been measured for deep-inelastic  $ep$  scattering [168] and quasi-elastic and deep-inelastic  $e-^3\text{He}$  scattering [169, 170], and comparison with available theory predictions is inconclusive as predictions vary up to two orders of magnitude depending on whether the two photons are assumed to couple with a single quark or two different quarks [166, 171], calling for experimental support to help distinguishing these model predictions. A run-group proposal [172] has been approved to measure the proton and the neutron TNSSA as part of the SoLID SIDIS running using transversely polarized  $\text{NH}_3$  and  $^3\text{He}$  targets, at the level of  $10^{-4} \sim 10^{-2}$ .

The BNSSA data, on the other hand, mostly existed for elastic scattering as it is a typical background of elastic PVES experiments. A compilation of elastic BNSSA data can be found in [173], along with new data from CREX/PREX-2 [174]. In contrast, BNSSA data for DIS is nearly non-existent, except for the previous 6 GeV PVDIS experiment [54] that measured

this asymmetry to 20 ppm level. A new proposal [10] has recently been approved to measure BNSSA for the proton in the DIS region to ppm level for the first time. The measurement will utilize a transversely polarized electron beam and SoLID in its PVDIS configuration. The value of BNSSA  $A_n$  will be extracted by fitting the measured asymmetry in the full azimuthal range to 2 and 4 ppm level for the 6.6 and 11 GeV beam, respectively. It will add a new, high-precision observable to the landscape of TPE study and its impact on the understanding of the nucleon structure.

### 7.5. PVDIS with a polarized $^3\text{He}$ target

All existing PVES, elastic or DIS, focused on measurements of the cross section asymmetries with the electron spin flip on an unpolarized target. On the other hand, parity violation would cause a cross section difference in unpolarized electron scattering off right- and left-handed, longitudinally polarized hadrons. Such new observable, referred to as ‘polarized parity-violating asymmetry’, can be written for the low to medium energy range as

$$A_{\text{pvdiss}}^{(h)} \approx \left( \frac{G_F Q^2}{2\sqrt{2}\pi\alpha} \right) \frac{g_V^e g_5^{\gamma Z} + Y g_A^e g_1^{\gamma Z}}{F_1^\gamma}, \quad (36)$$

where  $Y$  is given by equation (16), and we introduce polarized electroweak  $\gamma Z$  interference structure functions:

$$g_1^{\gamma Z} = \sum_i Q_q g_V^i (\Delta q_i + \Delta \bar{q}_i) \quad (37)$$

$$g_5^{\gamma Z} = \sum_f Q_q g_A^i (\Delta q_i - \Delta \bar{q}_i). \quad (38)$$

The  $g_5^{\gamma Z}$  contribution to the asymmetry, however, is suppressed since  $g_V^e \ll g_A^e$ . Thus our main focus will be on the first determination of the  $g_1^{\gamma Z}$ , which provides information on new flavor combination of polarized PDFs.

The flavor combination of the  $g_1^{\gamma Z}$  is rather unique and provides connections to our understanding of the nucleon spin. This can be seen if we take the approximation  $\sin^2 \theta_W \approx 0.25$ , giving

$$g_1^{p,\gamma Z} \approx g_1^{n,\gamma Z} \approx \frac{1}{9} (\Delta u^+ + \Delta c^+ + \Delta d^+ + \Delta s^+), \quad (39)$$

where  $\Delta q^+ \equiv \Delta q + \Delta \bar{q}$ . Therefore, the moment of  $g_1^{\gamma Z}$  provides approximately the total quark spin contribution to the proton spin, which is believed to be 30% [175].

The measurement of such asymmetry is more difficult than the PVDIS asymmetry of equation (11) (often referred to as ‘unpolarized PV asymmetry’), both because of the relatively small size of  $A_{pV}^{(h)}$  and because of the lower luminosity of polarized than unpolarized targets. A letter-of-intent [176] was submitted to JLab PAC in 2016 with the goal to measure the  $A_{pV}^{(h)}$  using a polarized  $^3\text{He}$  target and SoLID in the SIDIS configuration. To reach a high precision within a reasonable amount of beam time, the FOM of the polarized  $^3\text{He}$  target will need to be improved by factor 16 beyond its best-projected performance of the 12 GeV era, via the use of higher fill pressure of  $^3\text{He}$  and cryo-cooling to increase the in-beam density. The projected relative uncertainty is  $<10\%$  on  $A_{pV}^{(h)}$  for  $x = (0.2, 0.4)$ , using 180 d of production beam time at 100% efficiency. While technically challenging, it will be the first measurement of the  $g_1^{\gamma Z}$  structure functions. Similar measurements with the polarized proton could also be explored at the EIC.

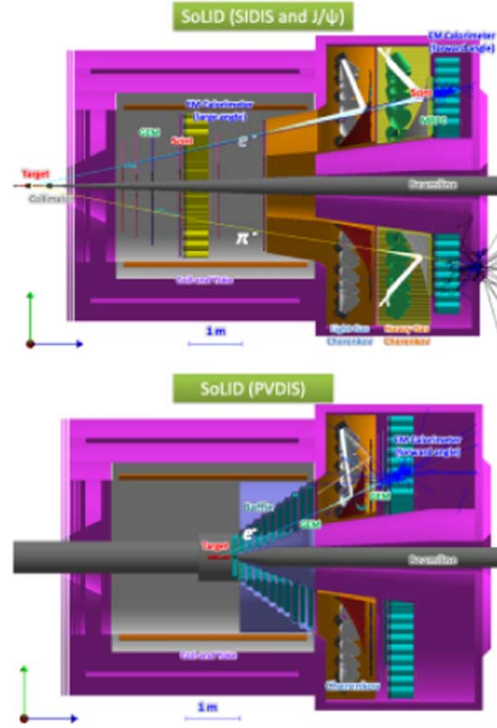


**Figure 28.** The two configurations of SoLID setup: SIDIS and  $J/\psi$  (top) and PVDIS (bottom).

## 8. SoLID instrumentation

### 8.1. Overview of SoLID setup

SoLID is a large acceptance spectrometer designed to handle a very high luminosity to exploit the full potential of the 12 GeV beam of CEBAF. The equipment of SoLID is designed to satisfy the physics requirements of the five approved experiments. It has the capacity to handle very high signal and background rates, and it can sustain the high radiation environment with a very high luminosity in JLab's experimental hall A.

A large solenoid magnet sweeps away low-energy background charged particles, which makes it possible to operate at very high luminosities in an open geometry with full azimuthal coverage. The solenoid field is also necessary for tracking and momentum measurement. The CLEO-II magnet has been selected with modifications to its iron flux return. The detector system of SoLID includes two configurations: the 'SIDIS& $J/\psi$ ' configuration and the 'PVDIS' configuration, as shown in figure 28.

The 'SIDIS& $J/\psi$ ' configuration consists of two groups of sub-detectors: the forward angle detector group (FAD), and the large angle detector group (LAD). The FAD group covers the nominal  $8^\circ$ – $15^\circ$  polar angle range and constitutes of five planes of GEMs for tracking, a light gas Čerenkov (LGC) for  $e/\pi$  separation, a heavy gas Čerenkov (HGC) for  $\pi/K$  and  $\pi/p$  separation, a MRPC for TOF measurement and for kaon and proton particle identifications, a scintillator pad detector (SPD) for photon rejection and a forward angle electromagnetic calorimeter (FAEC) for electron particle identification. The LAD group covers the nominal

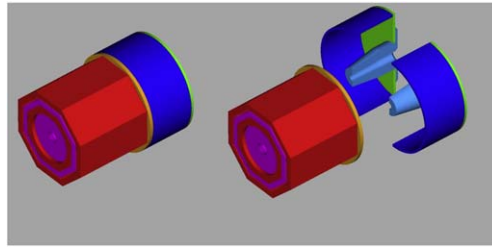


**Figure 29.** The endcap will be split vertically and also have the capability of separating in the lateral direction.

$15^{\circ}$ – $24^{\circ}$  polar angle range and constitutes of four planes of GEM for tracking, an SPD for photon rejection and a large angle electromagnetic calorimeter (LAEC) for electron particle identification. This configuration can work with luminosity of  $1 \times 10^{37} \text{ cm}^{-2} \cdot \text{s}^{-1}$ .

The ‘PVDIS’ configuration uses five GEM planes for tracking and LGC and EC for  $e/\pi$  separation to cover nominal  $22^{\circ}$ – $35^{\circ}$  polar angle range. It utilizes a set of baffles to reduce backgrounds while keeping a reasonable fraction of DIS electron events and can reach the luminosity of  $1 \times 10^{39} \text{ cm}^{-2} \cdot \text{s}^{-1}$ .

The two configurations share three major detector components: GEMs, LGC and EC. They also share similar data acquisition (DAQ) system, supporting structure for the magnet and the detectors, and software tools for simulations and data analysis.

There are additional components which are standard and existing at JLab that requires only slight modification, such as polarized  $\text{NH}_3$  and polarized  $^3\text{He}$  targets, and the standard cryogenic hydrogen target. There are other additional components which are required by the MOLLER experiment and will become available before SoLID is operational, such as a high-precision Compton polarimeter, a super-conducting Moller polarimeter, and an upgraded End Station Refrigerator (ESR2) that is needed by the higher-power cryogenic target of PVDIS.

The SoLID spectrometer can handle high rates with high background by using the latest detector, data acquisition and computing technologies. The following subsections will describe those detector components and technologies in details.

## 8.2. The CLEO-II magnet

A solenoid magnet is a natural choice to meet the needs of SoLID’s physics programs that require large acceptance in polar and azimuthal angles, and particle momentum. We have chosen the CLEO II’s solenoidal magnet, that has a uniform axial central field of 1.5 T, a large inner space with a clear bore diameter of 2.9 m and a coil of 3.1 m diameter. With a coil length of 3.5 m, its magnetic field uniformity is  $\pm 0.2\%$ . It was built in the 1980s by Oxford in England and installed for CLEO II in 1989 [177, 178]. After completion of experimental runs at Cornell, the coils and cryostat of the CLEO II magnet were moved to JLab in 2016 and the return steel moved in 2019. JLab is currently performing minor refurbishment of the magnet and preparing for a cold test to establish the magnet’s operational condition. The cold test is scheduled to be completed before the end of 2022.

To use the CLEO magnet for SoLID, the coil and upstream coil collar will be reused as-is but the downstream coil collar and return yoke will be modified. A new detector endcap and front pieces will be fabricated that allow housing and installation of the detectors, see figure 29.

### 8.3. GEM trackers

Particle tracking for SoLID will be performed by GEM trackers [179]. The GEM trackers are ideal for the SoLID detector because they provide for high resolution tracking and can operate in high-rate environments over a large area. More specifically, we expect the GEMs to provide a position resolution of  $70\ \mu\text{m}$  with rates over  $100\ \text{MHz per cm}^2$ . The current design of SoLID GEM chambers call for a triple design: each chamber is made of three GEM foils sandwiched between a drift area and a readout plane. Such triple GEM chambers have been successfully used in the COMPASS experiment at CERN [180], and in the PRad experiment at JLab [181]. A large set of triple GEM detectors of the size comparable to those needed for SoLID is currently used for the SBS program in Jlab Hall A. These SBS GEMs have performed very well in beam yielding highly stable operation. In SBS experiments, these GEMs will be exposed to rates comparable to those expected in SoLID experiments.

For the PVDIS configuration, five layers of GEMs will be used, each layer consisting of 30 sectors in the azimuthal direction that match the baffle design. This layout will allow for a  $1\ \text{mrad}$  polar angle and a  $2\%$  momentum resolutions.

The SIDIS configuration of SoLID calls for six layers of GEM modules. The SIDIS GEM will be assembled using the same GEM modules used in the PVDIS configuration. Because of the different coverage area required by SIDIS compared with PVDIS, this re-arrangement will allow small overlapping between GEM chambers, minimizing the acceptance loss due to inactive area caused by GEM chamber frames. In the PVDIS configuration these frames sit in the shadows of the baffle-ribs and do not contribute to any loss of acceptance.

### 8.4. Light gas Cherenkov detector

The LGC detector provides electron identification in both SIDIS+ $J/\psi$  and PVDIS configurations. The LGC is comprised of a tank of  $\text{CO}_2$  gas as radiator is divided into 30 sectors, each consisting of a pair of mirrors and one readout assembly onto which light is reflected. Each readout assembly is made of 9 Hamamatsu flat panel multianode photomultipliers (MAPMT) H12700-03 in a  $3 \times 3$  array. Those MAPMT will be coated with a p-terphenyl wavelength shifter to enhance the efficiency of UV light detection. The MAPMTs have 64 pixels, each of which is sensitive down to single photon detection. Their signals can be read out individually or as sum of 16 pixels (quad-sum) or as the sum of all 64 pixels (total-sum). With these design features, the LGC is expected to have a nominal pion rejection on the order of  $10^3$  while maintaining an electron efficiency close to  $95\%$ . It will be part of electron trigger system.

A parasitic beam test was conducted on an Cherenkov prototype at JLab Hall-C in 2020. The prototype telescopic Cherenkov device (TCD) was built with the same electronic components expected for use in the SoLID LGC. It used a UV mirror to collect light from  $1\ \text{m}$  long  $\text{CO}_2$  gas onto a  $4 \times 4$  WLS-coated MAPMT array. The device was tested at high rates that reached about twice the maximum rate expected during SoLID production running. The TCD performed within expectations at these large rates and the trigger capability using either quad-sum or total-sum were verified.

### 8.5. Heavy gas Cherenkov detector

For the SIDIS experiments, the HGC detector will identify charged pion and suppress charged kaon for a momentum range from  $2.5$  to  $7.5\ \text{GeV c}^{-1}$  at the forward angle. Its radiator will be  $1\ \text{m}$  length of the heavy gas  $\text{C}_4\text{F}_8$  at  $1.7\ \text{atm}$  absolute pressure at the room temperature of  $20\ \text{C}$ . Matching LGC and covering the full azimuthal angle, it will have 30 sectors. Each



sector has one spherical mirror to collect lights onto a  $4 \times 4$  MaPMT arrays which are surrounded by a light collection cone and magnetic shielding cone. The HGC mirror, MaPMT and readout electronics are similar to the components of LGC, but HGC will not be part of the trigger system. The detector is expected to have a pion detection efficiency of 90% and a kaon rejection of 10. During the Cherenkov beam test at JLab Hall-C in 2020, the Cherenkov prototype was tested with  $C_4F_8$  gas at 1 atm and it performed within expectations. Additionally, a full-size 4-sector HGC prototype was designed and constructed with an Aluminum thin front window to test the operating pressure of 1.7 atm. This test showed the current design maintains mechanical stability with negligible leakage.

### 8.6. Electromagnetic calorimeter

The segmented electromagnetic calorimeter (ECal) consists of a preshower and a shower section, and will be used as the primary electron trigger and identification during all experiments. The preshower portion consists of a  $2X_0$  pre-radiator and a 2 cm thick scintillator with wave-length shifting (WLS) fibers embedded for light readout. The shower portion is  $18X_0$  long, based on the Shashlyk-type sampling [182] with alternating layers of 1.5 mm thick scintillator and 0.5 mm thick lead absorber layers. The choice of the sampling-type design was mostly driven by a balance between cost and the required radiation hardness. The layout of ECal models will be different between the two SoLID configurations: The SIDIS+ $J/\psi$  configuration will have the ECal at both forward and large-angle regions for electron detection with the large-angle ECal also providing MIP triggers for pions. The PVDIS configuration will have all ECal modules at the forward direction to detect DIS electrons. There will be approximately 1800 modules, each with a transverse size  $100\text{ cm}^2$  in a hexagon shape such that they can be rearranged between the two configurations. A unique aspect of SoLID's ECal is its light readout: because of the high radiation nature of SoLID's operation, all WLS fibers will be connected to clear fibers and light will be routed outside of the solenoid magnet for readout by PMTs. Radiation hardness of a variety of WLS and clear fibers has been measured and is found to be sufficient to sustain the SoLID physics program.

A number of prototypes have been constructed for the SoLID ECal preshower and shower modules and their light yield studied with both cosmic rays and particle beams. Using the Fermilab Test Beam Facility, the energy resolution of the ECal prototype was found to satisfy the needs of the SoLID physics program. Tests with the electron beam at JLab are ongoing to further study the ECal performance under the high-rate, high background environment.

### 8.7. Scintillator pad detector

The SPD will be used at both forward-angle and large-angle locations of the SIDIS configuration to provide photon rejection at the 5:1 and 10:1 level, respectively, and to reduce ECal-based trigger rates by requiring coincidence signals between the SPD and the ECal. The forward-angle SPD will be made of 240 pieces of thin, large scintillator pads with WLS fibers embedded on the surface. Light from the WLS fibers will be guided through clear fibers in a similar manner as the preshower ECal. The large-angle SPD (LASPD) also provides TOF with a timing resolution goal of 150 ps, and as a result are made of 2 cm thick long, wedge shape scintillators with readout directly by field-resistant fine-mesh PMT on the edge of the solenoid field. The fine-mesh PMTs have been tested under a magnetic field up to 1.9 T and its gain and timing resolution characterized [183]. The SPD prototype modules have been tested with cosmic rays. We found that the fine-mesh PMTs combined with the LASPD can provide a 150 ps timing resolution as specified by the SoLID SIDIS program. Tests with the



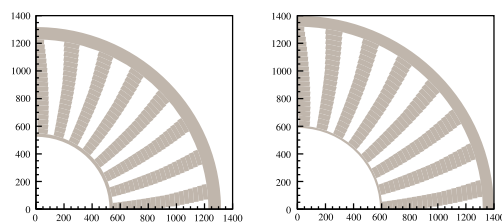


**Figure 30.** Face on view (first quadrant only) of the 10th and 11th plates in the PVDIS baffle system. Units are in mm.

electron beam at JLab are ongoing to further study the SPD performance under the high-rate, high background environment.

### 8.8. Multi-gap resistive plate chamber

The MRPC, which will be used as the TOF system in the SIDIS configuration, is located in front of the forward angle ECal. The unique advantage of the MRPC is that it not only can operate in a strong magnetic field, but also can handle extreme high rates. The new generation sealed MRPC developed by Tsinghua University can reach the rate capability as high as  $50 \text{ kHz cm}^{-2}$  utilizing a new type of low resistivity glass (in the order of  $10 \Omega \text{ cm}$ ) [184–187]. On top of that, the MRPC designed for SoLID has a thin gas gap of  $104 \mu\text{m}$  with 8 gaps per stack and a total of 4 stacks [151]. A cosmic ray test on two identical  $4 \times 8$  gaps MRPCs conducted at Tsinghua University with a  $5 \text{ GS s}^{-1}$  waveform digitizer shows a time resolution of 27 ps. Simulation shows that the intrinsic time resolution of such an MRPC can be as better as 14 ps using a much higher sampling rate ( $\sim 10 \text{ GS s}^{-1}$ ) front-end electronics (FEE). With a total path length of 8 meters in the SIDIS configuration, the MRPC with a time resolution of 20 (30) ps can identify pions from kaons with momenta up to 7 (6)  $\text{GeV c}^{-1}$ . The studies of the MRPC's realistic performance with several fast FEE candidates are ongoing using real high-energy beams at Fermilab and JLab.

### 8.9. Baffles for PVDIS

In order for the detectors in the PVDIS experiment to operate at the design luminosity, a set of baffles11 slitted plates made of an absorber material is designed such that a reasonable fraction of the DIS electrons pass through the slits. The slits in the multiple layers of the baffle system provide curved channels through which only spiraling high-energy charge-negative particles can pass, while low-energy and charge-neutral or charge-positive backgrounds are highly suppressed.

To design the baffles for a specific magnetic field and detector configuration, ray-tracing of simulated DIS electrons is performed for the desired momentum range. The number of sectors to be used for the PVDIS experiment is driven by the azimuthal angle  $\phi$  traversed by the minimum momentum particles, which for the desired DIS kinematics is about  $12^\circ$ , hence the baffles are divided into 30 sectors. Segmentation of all detector system have the same number of sectors to match the baffle design. An illustration of the first 5 layers of the baffle system is given in figure 30. In practice, the simple ray-tracing model does not completely hold because the target has an extended length, allowing some fraction of background events to leak through.

Three different material choices are being considered for the baffles. The baseline design is based on lead. Two other alternatives are tungsten power molded and glued to the desired

shape, and copper. All will meet the requirement of PVDIS and with small differences in the resulting photon and hadron background rates. Additional care is taken to reduce secondary particles, such as those produced from photons hitting the baffle near the slits. Studies are being carried out on activation of the material and feasibility in construction will be taken into account. Overall, the baffles are expected to allow about 1/3 of DIS events to reach the detectors, while background events are suppressed by two orders of magnitude.

#### 8.10. Support and infrastructure

The solenoid magnet will be supported on a stationary frame that will distribute the approximate 1000 ton load of the modified CLEO-II magnet section using eight 200 ton energpac jacks. Steel plates and large steel blocks and/or large I-beams will be used to distribute the load over a safe area. The 200 ton jacks will be used for vertical alignment and have locking rings which allow for a full mechanical connection and not rely on hydraulic pressure for stationary support.

The endcap of the magnet will have a support structure that cradles each half the cylindrical ring. The structure will be integrated into a track system that is mounted to steel plates resting upon the concrete floor of Hall A. The track system will consist of a set of longitudinal tracks for moving the rear plate and nose unit of the endcap downstream away from the magnet. A set of lateral tracks will separate the two endcap cylindrical halves that support the detectors and move each away from the beamline. Motion can be achieved by using hydraulic or electric cylinders to push and pull the entire system into position.

Inside the magnet bore, the insertion of the SIDIS large angle detector packages that reside internal to the cryostat will be accomplished from the downstream side of the magnet using a supporting framework to roll the packages in and out. This will require the detector hut to be moved out of the way as described above to allow access to the cryostat. In the inner bore region, an internal frame system is needed to mount the baffles in the PVDIS configuration and the large angle detectors for the SIDIS configuration. The frame cannot come into contact with the inside bore of the cryostat. This requires the frame to span the entire length of the cryostat and mount to the return yoke iron. A stainless steel support cylinder will be mounted between the two coil collars to bridge across the length of the cryostat. Individual rails will bolt directly to the stainless cylinder to allow the internal detector packages to roll into place. The same rail system can be used for both configurations as well as the detectors in the endcap. A large universal installation fixture is envisioned to load each of the detector packages onto the rails of the magnet and endcap.

#### 8.11. Event rates and data acquisition

The trigger rates were simulated with the full background. The SIDIS configuration, with an expected trigger rate of 100 kHz and total data rate of over  $3 \text{ GB s}^{-1}$ , represents the greatest challenge for SoLID's data acquisition (DAQ) system. The PVDIS rates are also high, but are not as demanding as they are divided into 30 sectors with each equipped with individual DAQs. The SoLID DAQ is mostly based on JLab250 FADCs for the readout of PMTs of ECal and Cherenkov detectors. These electronics provide both readout and trigger capability on any detector fed into the FADCs. The FADC readout so far has been shown to be able to operate up to 120 KHz of trigger rate at around 1% of deadtime satisfying the SIDIS requirements. The GEM readout will use the VMM3 which has a minimum rate capability of 100 kHz at full occupancy. So far, the SoLID DAQ system which can handle data rates of several GB/s is feasible using technology currently in use at JLab.

**Table 1.** Estimated SoLID computing requirements. CPU times are calculated assuming AMD EPYC 7502 processors.

Experiment	SIDIS $^3\text{He}$ (T)	SIDIS $^3\text{He}$ (L)	SIDIS $\text{NH}_3$ (T)	$J/\psi$	PVDIS
Storage (PB)	26	10	35	21	95
CPU time (M-core-hrs)	30	12	40	17	134

### 8.12. Computing

Estimated computing needs for SoLID are summarized in table 1. These are total resource requirements over the lifetime of the experiment, assuming that all simulation and production output is kept. Total overall resources needed are 188 PB storage and 233 M-core-hours CPU. This corresponds to 485 d of processing time on a 20 000 core cluster.

To arrive at the numbers in table 1, average trigger rates of 100 kHz for the SIDIS experiments, 60 kHz for  $J/\psi$ , and 20 kHz per sector for PVDIS, are assumed (see section 8.11). Event size estimates come from simulations and are 20 kB for SIDIS, 40 kB for  $J/\psi$ , and 6 kB per sector for PVDIS. The resulting instantaneous raw data rates range from 2.0 to 3.6 GB s<sup>-1</sup>.

### 8.13. Software

Software developed for SoLID to date comprises three main projects

- (i) `SOLID_GEMC` [188], a simulation package built on GEMC [189], a generic simulation framework used by CLAS12 and other projects at JLab. GEMC is based on Geant4 [190].
- (ii) `libsolgem`, a digitization package for GEM detectors, which was developed by the SoLID collaboration [191].
- (iii) `SoLIDTracking`, a library of experimental track reconstruction routines for the three main configurations of SoLID [192]. This package employs a Kalman filter algorithm and is based in part on prior implementations for experiments at KEK and GSI.

A detailed description of packages ii and iii can be found in [193], which also includes a study of efficiency and accuracy of the track reconstruction algorithm applied to simulated data from `SOLID_GEMC`.

The long-term goal for SoLID software development is to put in place a unified end-to-end simulation and reconstruction framework, which will provide an integrated software environment for (almost) all parts of data processing. Implementing a software ecosystem for a new experiment requires considerable effort. In light of limited staffing, it will be necessary to adopt preexisting components wherever possible. At present, the most fruitful approach appears to be for SoLID software to be closely aligned with that of the EIC project.

### 8.14. Advancing detector technology

SoLID is designed to carry out experiments with high rate and high background. For many experiments, the luminosity achievable is limited by the detector occupancies. We are investigating new detector technologies with faster response time to improve the rate capability of SoLID. The large area picosecond photodetector (LAPPD) is being developed by

INCOM and Argonne National Lab: it is a novel, affordable large area Microchannel Plate Photomultiplier (MCP PMT) and was tested in beam [194]. The pulse width of MCP PMT is of the order of 1 ns compared to about 20 ns for a regular PMT, possibly reducing greatly the pile-up for the Cherenkov detectors. This technology, when it becomes mature, would be a prime candidate as photosensor for the Cherenkov readouts.

Another technology being considered is the superconducting nano-wire technology [195]. The detector exhibits excellent timing resolution and is likely to be more radiation harder than traditional technology. Such a detector could be used to complement the GEM tracking as a vertex tracker or provide additional tracking planes.

## 9. Opportunities with future upgrades of CEBAF

### 9.1. $J/\psi$ and $\psi'$ Production with 20<sup>+</sup> GeV

A CEBAF energy upgrade to 20 GeV or higher would enable several additional topics to be pursued with the SoLID- $J/\psi$  setup. The electroproduction measurement at larger beam energies could operate without any changes to the 11 GeV setup, although further optimizations could be considered. A beam energy of 20 GeV or higher would access values of  $Q^2$  up to 10 GeV<sup>2</sup> or larger, providing an additional large scale to aid with factorization. The photoproduction measurement would allow for a precision measurement of  $J/\psi$  cross section at slightly larger energies, superseding the previous SLAC [196] and Cornell [197] measurements. Furthermore, this would enable a small overlap region with the measurements at the EIC, where the SoLID measurement would have much a higher resolution in  $W$  and a unique reach to high  $t$  that cannot be done anywhere else. Finally, a measurement at higher energies allows a simultaneous measurement of  $J/\psi$  and  $\psi'$  production, where the latter process provides for an independent knob to constrain the gluonic physics inside the proton, as it is a larger-size color dipole.

Projected 1D and 2D cross section results for  $\psi'$  production with SoLID at 20 GeV are shown in figures 31 and 32.

### 9.2. Nucleon 3D structure with 20<sup>+</sup> GeV

The SIDIS and GPD programs of SoLID will also benefit from the CEBAF energy upgrade to 20 GeV or higher, resulting in significantly extended kinematic coverage of observables and potentially open up new physics channels for the nucleon 3D structure study. Figure 33 shows the simulated  $Q^2$ - $x$  phase-space with various beam energies from 11 to 24 GeV using the SIDIS configuration of SoLID with a polarized <sup>3</sup>He target.

Preliminary studies have been carried out for the Collins SSA, as shown in figure 34. A few  $Q^2$ - $z$  bins were selected from the full coverage of  $2.0 < Q^2 < 20.0$  GeV<sup>2</sup> and  $0.30 < z < 0.70$ . As expected, SoLID with a higher energy beam of CEBAF will provide precision measurements of SIDIS and GPD in the higher  $Q^2$  and lower  $x$  region, that cannot be charted with the 12 GeV beam.

More detailed studies, including those for the proton target and for other physics channels, will be carried out to optimize the potential physics programs of SoLID with a higher energy beam.

### 9.3. Electroweak physics with a positron beam

With a higher beam energy of 20 GeV or above, the PVDIS measurements can be extended to higher  $Q^2$ , providing improved precision on the  $\sin^2 \theta_W$  and the  $2g_{VA}^{eu} - g_{VA}^{ed}$  coupling, or the

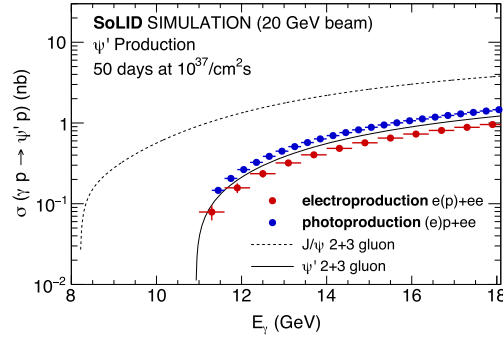


**Figure 31.** Projected 1D cross section results for  $\psi'$  production assuming a 20 GeV beam energy and the nominal SoLID- $J/\psi$  experimental setup without any optimization for the higher beam energy, for 50 d at  $10^{37} \text{ cm}^{-2} \text{ s}^{-1}$ . The blue disks show the photoproduction results and the red disks the electroproduction results.

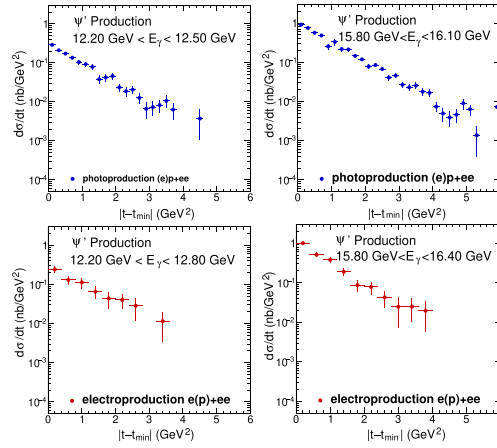


**Figure 32.** Top row: The projected differential cross section for a photoproduction bin at low (left) and high (right) photon energy from figure 31, assuming the nominal luminosity for SoLID- $J/\psi$  with a beam energy of 20 GeV. Bottom row: Same for two electroproduction bins. This figure illustrates that a precise measurement of the  $t$ -dependence for  $\psi'$  production is possible with the nominal SoLID- $J/\psi$  setup at higher energies.

PDF ratio  $d/u$  for higher  $x$ . On the other hand, the addition of a positron beam at CEBAF will open up a wide range of physics topics not accessible with an electron beam alone [163]. One new observable that we can measure with SoLID and a positron beam is the lepton-charge asymmetry, defined as the cross section asymmetry between positron and electron DIS:

$$A^{e^+e^-} \equiv \frac{\sigma^{e^+} - \sigma^{e^-}}{\sigma^{e^+} + \sigma^{e^-}}, \quad (40)$$

and is related to the neutral current coupling,  $g_{AA}^{eq}$ , predicted by the SM as  $g_{AA}^{eq} = 2g_A^e g_A^q$  and  $g_{AA}^{eu} = -g_{AA}^{ed} = -1/2$ . More specifically, the asymmetry  $A^{e^+e^-}$  between unpolarized  $e^+$  and  $e^-$  beams deep-inelastic-scattering off an isoscalar target has an electroweak contribution that is

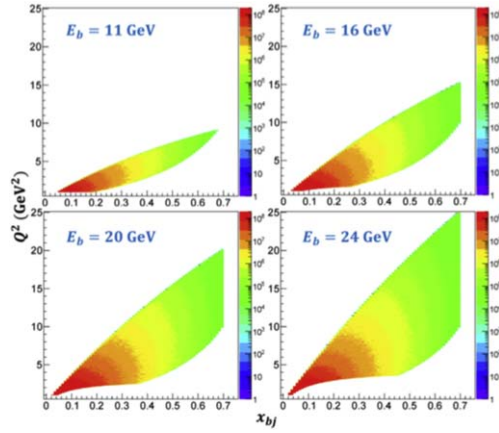


**Figure 33.** Projected kinematic coverage of SoLID-SIDIS with polar angles from  $5^\circ$  to  $27^\circ$  for various beam energies. The projections were simulated with a  $^3\text{He}$  target and the SoLID acceptance effects were turned off. The polar angle range,  $5^\circ$ – $27^\circ$ , was optimized for the upgraded CEBAF energy.

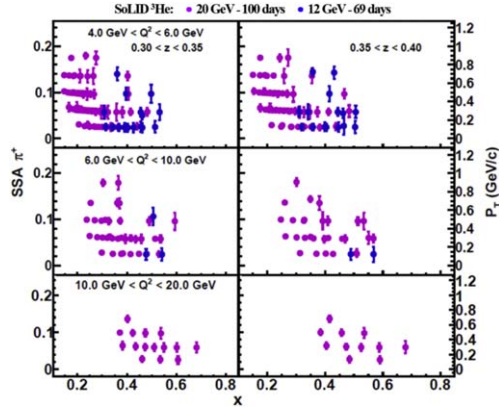


**Figure 34.** Selected  $Q^2$ - $z$  bins of projected Collins SSA with SoLID-SIDIS configuration and  $^3\text{He}$  target. Two different beam energies, 12 GeV and 20 GeV, are included to compare their kinematic coverage.

directly proportional to the combination  $2g_{AA}^{eu} - g_{AA}^{ed}$  [63]:

$$A^{e^+e^-} = -\frac{3G_F Q^2}{2\sqrt{2}\pi\alpha} Y \frac{R_V}{5} (2g_{AA}^{eu} - g_{AA}^{ed}), \quad (41)$$

where  $R_V$  was defined in section 4 and the effect of sea quarks has been omitted for SoLID's kinematic coverage. Such measurement [198], if successful, would provide the first measurement of this coupling for the electrons, superseding the previous measurement using muon beams at CERN [199] that gave  $2g_{AA}^{\mu u} - g_{AA}^{\mu d} = 1.57 \pm 0.38$ .

The measurement of  $A^{e^+e^-}$  faces both experimental and theoretical challenges. Experimentally, differences in beam energy, intensity, and the detection of the scattered particles between  $e^+$  and  $e^-$  runs will cause sizable contributions to  $A^{e^+e^-}$ , though these effects have a

calculable kinematic-dependence and could be separated from electroweak contributions. Theoretically, electromagnetic interaction causes an asymmetry between  $e^+$  and  $e^-$  scatterings at the next-to-leading and higher orders, causing a contribution to  $A^{e^+e^-}$  that are significantly larger than the electroweak contribution at the  $Q^2$  values of JLab. Progress in theory is needed in the coming decade to describe  $A^{e^+e^-}$  at the level of precision required by the  $g_{AA}^{eq}$  measurement.

## 10. Summary

The SoLID spectrometer is a multi-purpose device that can address many of the central issues in the studies of QCD and fundamental symmetries. Three SIDIS experiments to perform precision measurements with transversely and longitudinally polarized  $^3\text{He}$  (effective polarized neutron) and transversely polarized proton will allow precision extractions of TMDs in the valence quark region to map out the 3D structure of the nucleon in momentum space. An experiment of electro- and photo-production of  $J/\psi$  near threshold region probes the gluonic field and its contribution to the proton mass. A parity-violating DIS experiment will determine the effective electron-quark couplings of the Standard Model, pushing the limits in phase space in search for new physics, and will provide the PDF ratio  $d/u$  at high  $x$ . A number of run-group experiments have been approved, including the exploration of GPDs with deep exclusive reactions to study the 3D structure of the nucleon in coordinate space. At the latest JLab PAC meeting in 2022, all five SoLID experiments were re-approved with the highest rating (A) and two new experiments were added, including a measurement to study two photon exchange effects and a measurement to study isospin dependence of the EMC effect. The key to the high impact of each of these experiments is the high luminosity combined with the large acceptance of SoLID, with orders of magnitudes higher figure-of-merit than all other devices at existing and future  $ep$  (and  $eA$ ) facilities. SoLID will thus exploit the full potential of the JLab-12 GeV beam, with a kinematic reach complementary to that of EIC. The design of SoLID has been vetted by several JLab Director's reviews and a DOE Science Review. It shares significant synergy with EIC including detector technology, simulation, data acquisition capacity, software integration, data analysis aided by artificial intelligence and machine learning, radiative corrections and unfolding, and finally, training of the nuclear physics workforce for the QCD and fundamental symmetry frontier for the next decades.

## Acknowledgments

This material is based upon work supported in part by the US Department of Energy, Office of Science, and Office of Nuclear Physics under contract numbers DE-AC05-06OR23177 (JLab), DE-AC02-06CH11357 (ANL), DE-FG02-03ER41231 (Duke), DE-FG02-96ER40988 (Stony Brook U), DE-FG02-84ER40146 (Syracuse U), DE-FG02-94ER40844 and DE-SC0016577 (Temple U), DE-SC00-14434 (U of Virginia); and Office of Science, Office of Workforce Development for Teachers and Scientists (WDTS) under the Science Undergraduate Laboratory Internships Program. Z -H Ye thanks Tsinghua University Initiative Scientific Research Program for the support. We thank A Accardi, S Kuhn, and S Mantry for the useful discussions that contributed to this manuscript.



## Data availability statement

No new data were created or analysed in this study.

## ORCID iDs

J Arrington  <https://orcid.org/0000-0002-0702-1328>  
 G Evans  <https://orcid.org/0000-0001-7612-9490>  
 J-O Hansen  <https://orcid.org/0000-0002-7908-3886>  
 G M Huber  <https://orcid.org/0000-0002-5658-1065>  
 Z-E Meziani  <https://orcid.org/0000-0001-9450-2914>  
 W Xiong  <https://orcid.org/0000-0002-7315-3986>

## References

- [1] Chen J P *et al* (SoLID collaboration) A white paper on SoLID (solenoidal large intensity device) arXiv:1409.7741
- [2] The SoLID Collaboration 2019 Solenoidal large intensity device updated preliminary conceptual design report <https://solid.jlab.org/DocDB/0002/000282/001/solid-precdr-2019Nov.pdf>
- [3] Arrington J *et al* Physics with CEBAF at 12 GeV and future opportunities arXiv:2112.00060
- [4] Chen J-P *et al* Target single spin asymmetry in semi-inclusive deep-inelastic ( $e, e'\pi^\pm$ ) reaction on a transversely polarized  $^3\text{He}$  target at 11 GeV Jefferson Lab Experiment E12-10-006, 2010 with 2022 update
- [5] Chen J-P *et al* Asymmetries in semi-inclusive deep-inelastic ( $e, e'\pi^\pm$ ) reactions on a longitudinally polarized  $^3\text{He}$  target at 8.8 and 11 GeV Jefferson Lab Experiment E12-11-007, 2011 with 2022 update
- [6] Chen J-P *et al* Target single spin asymmetry in semi-inclusive deep-inelastic ( $e, e'\pi^\pm$ ) reaction on a transversely polarized proton target Jefferson Lab Experiment E12-11-108, 2011 with 2022 update
- [7] Joosten S *et al* Near threshold electroproduction of  $J/\Psi$  at 11 GeV Jefferson Lab Experiment E12-12-006, 2012 with 2022 update
- [8] Souder P A *et al* 2022 Precision measurement of parity-violation in deep inelastic scattering over a broad kinematic range Jefferson Lab Experiment E12-10-007, 2010 with 2022 update
- [9] Arrington J *et al* 2022 First measurement of the flavor dependence of nuclear PDF modification using parity-violating deep inelastic scattering Jefferson Lab Proposal PR12-22-002
- [10] Nycz M *et al* 2022 Measurement of the beam normal single spin asymmetry in deep inelastic scattering using the SoLID spectrometer Jefferson Lab Experiment E12-22-004
- [11] Huber G M *et al* 2017 Measurement of deep exclusive  $\pi^-$  production using a transversely polarized  $^3\text{He}$  target and the SoLID spectrometer Jefferson Lab Run Group Experiment E12-10-006B
- [12] Boer M *et al* 2015 Timelike Compton scattering on the proton in  $e^+e^-$  pair production with SoLID at 11 GeV Jefferson Lab Run Group Experiment E12-12-006A
- [13] Ethier J J and Nocera E R 2020 Parton distributions in nucleons and nuclei *Ann. Rev. Nucl. Part. Sci.* **70** 43–76
- [14] Metz A and Vossen A 2016 Parton fragmentation functions *Prog. Part. Nucl. Phys.* **91** 136–202
- [15] Belitsky A V, Ji X-D and Yuan F 2004 Quark imaging in the proton via quantum phase space distributions *Phys. Rev. D* **69** 074014
- [16] Lorce C and Pasquini B 2011 Quark wigner distributions and orbital angular momentum *Phys. Rev. D* **84** 014015
- [17] Gao H *et al* 2011 Transverse spin structure of the nucleon through target single spin asymmetry in semi-inclusive deep-inelastic ( $e, e'\pi^\pm$ ) reaction at Jefferson lab *Eur. Phys. J. Plus* **126** 2
- [18] Mulders P J and Tangerman R D 1996 The complete tree level result up to order  $1/Q$  for polarized deep inelastic leptonproduction *Nucl. Phys. B* **461** 197–237

- [19] Boer D and Mulders P J 1998 Time reversal odd distribution functions in leptonproduction *Phys. Rev. D* **57** 5780–6
- [20] Jaffe R L and Ji X-D 1991 Chiral odd parton distributions and polarized Drell-Yan *Phys. Rev. Lett.* **67** 552–5
- [21] Barone V, Drago A and Ratcliffe P G 2002 Transverse polarisation of quarks in hadrons *Phys. Rep.* **359** 1–168
- [22] D’Alesio U, Flore C and Prokudin A 2020 Role of the Soffer bound in determination of transversity and the tensor charge *Phys. Lett. B* **803** 135347
- [23] Bastami S *et al* 2019 Semi-inclusive deep inelastic scattering in Wandzura–Wilczek-type approximation *J. High Energy Phys.* **JHEP06(2019)007**
- [24] Collins J C 1993 Fragmentation of transversely polarized quarks probed in transverse momentum distributions *Nucl. Phys. B* **396** 161–82
- [25] Abe K *et al* (Belle collaboration) 2006 Measurement of azimuthal asymmetries in inclusive production of hadron pairs in  $e^+e^-$  annihilation at Belle *Phys. Rev. Lett.* **96** 232002
- [26] Huang J *et al* (Jefferson Lab Hall A collaboration) 2012 Beam-target double spin asymmetry  $A_{LT}$  in charged pion production from deep inelastic scattering on a transversely polarized  $^3\text{He}$  target at  $1.4 < Q^2 < 2.7$  GeV<sup>2</sup> *Phys. Rev. Lett.* **108** 052001
- [27] Anselmino M, Mukherjee A and Vossen A 2020 Transverse spin effects in hard semi-inclusive collisions *Prog. Part. Nucl. Phys.* **114** 103806
- [28] Chen J-P *et al* 2014 Dihadron electroproduction in DIS with transversely polarized  $^3\text{He}$  target at 11 and 8.8 GeV Jefferson Lab Run Group Experiment E12-10-006A
- [29] Liu T *et al* 2018  $K^\pm$  production in semi-inclusive deep inelastic scattering using transversely polarized targets and the SoLID spectrometer Jefferson Lab Run Group Experiment E12-10-006D/E12-11-108B
- [30] Qian X *et al* (Jefferson Lab Hall A collaboration) 2011 Single spin asymmetries in charged pion production from semi-inclusive deep inelastic scattering on a transversely polarized  $^3\text{He}$  target *Phys. Rev. Lett.* **107** 072003
- [31] Anselmino M and Prokudin A private communication
- [32] Ye Z *et al* 2017 Unveiling the nucleon tensor charge at Jefferson Lab: a study of the SoLID case *Phys. Lett. B* **767** 91–8
- [33] Aoki S *et al* (Flavour Lattice Averaging Group Collaboration) 2020 FLAG review 2019: flavour lattice averaging group (FLAG) *Eur. Phys. J. C* **80** 113
- [34] Gupta R *et al* (Precision Neutron Decay Matrix Elements (PNDME) Collaboration) 2018 Isovector charges of the nucleon from  $2 + 1 + 1$ -flavor lattice QCD *Phys. Rev.* **98** 034503
- [35] Alexandrou C *et al* 2020 Nucleon axial, tensor, and scalar charges and  $\sigma$ -terms in lattice QCD *Phys. Rev. D* **102** 054517
- [36] Gamberg L *et al* (Jefferson Lab Angular Momentum (JAM) Collaboration) 2022 Updated QCD global analysis of single transverse-spin asymmetries: extracting  $\tilde{H}$ , and the role of the soffer bound and lattice QCD *Phys. Rev. D* **106** 034014
- [37] Cammarota J *et al* (Jefferson Lab Angular Momentum (JAM) Collaboration) 2020 Origin of single transverse-spin asymmetries in high-energy collisions *Phys. Rev. D* **102** 054002
- [38] Gamberg L, Kang Z-B, Pitonyak D, Prokudin A, Sato N and Seidl R 2021 Electron-ion collider impact study on the tensor charge of the nucleon *Phys. Lett. B* **816** 136255
- [39] Ellis J R and Flores R A 1996 Implications of the strange spin of the nucleon for the neutron electric dipole moment in supersymmetric theories *Phys. Lett. B* **377** 83–8
- [40] Bhattacharya T, Cirigliano V and Gupta R 2012 Neutron electric dipole moment from beyond the standard model *Proc. Sci.* **LATTICE2012** 179
- [41] Pitschmann M, Seng C-Y, Roberts C D and Schmidt S M 2015 Nucleon tensor charges and electric dipole moments *Phys. Rev. D* **91** 074004
- [42] Xu S-S, Chen C, Cloet I C, Roberts C D, Segovia J and Zong H-S 2015 Contact-interaction Faddeev equation and, inter alia, proton tensor charges *Phys. Rev. D* **92** 114034
- [43] Liu T, Zhao Z and Gao H 2018 Experimental constraint on quark electric dipole moments *Phys. Rev. D* **97** 074018
- [44] Pospelov M and Ritz A 2005 Electric dipole moments as probes of new physics *Ann. Phys.* **318** 119–69
- [45] Prescott C Y *et al* 1978 Parity nonconservation in inelastic electron scattering *Phys. Lett. B* **77** 347–52

- [46] Prescott C Y *et al* 1979 Further measurements of parity nonconservation in inelastic electron scattering *Phys. Lett. B* **84** 524–8
- [47] Armstrong D S *et al* (G0 collaboration) 2005 Strange quark contributions to parity-violating asymmetries in the forward G0 electron–proton scattering experiment *Phys. Rev. Lett.* **95** 092001
- [48] Androic D *et al* (G0 collaboration) 2010 Strange quark contributions to parity-violating asymmetries in the backward angle G0 electron scattering experiment *Phys. Rev. Lett.* **104** 012001
- [49] Adhikari D *et al* (PREX collaboration) 2021 Accurate determination of the neutron skin thickness of  $^{208}\text{Pb}$  through parity-violation in electron scattering *Phys. Rev. Lett.* **126** 172502
- [50] Androic D *et al* (Qweak collaboration) 2013 First determination of the weak charge of the proton *Phys. Rev. Lett.* **111** 141803
- [51] Androic D *et al* (Qweak collaboration) 2018 Precision measurement of the weak charge of the proton *Nature* **557** 207–11
- [52] Young R D, Carlini R D, Thomas A W and Roche J 2007 Testing the standard model by precision measurement of the weak charges of quarks *Phys. Rev. Lett.* **99** 122003
- [53] Wang D *et al* (PVDIS collaboration) 2014 Measurement of parity violation in electron–quark scattering *Nature* **506** 67–70
- [54] Wang D *et al* 2015 Measurement of parity-violating asymmetry in electron–deuteron inelastic scattering *Phys. Rev. C* **91** 045506
- [55] Benesch J *et al* (MOLLER collaboration) The MOLLER experiment: an ultra-precise measurement of the weak mixing angle using Möller scattering arXiv:1411.4088
- [56] Becker D *et al* 2018 The P2 experiment *Eur. Phys. J. A* **54** 208
- [57] Davoudiasl H, Lee H-S and Marciano W J 2014 Muon  $g-2$ , Rare Kaon decays, and parity violation from dark Bosons *Phys. Rev. D* **89** 095006
- [58] Davoudiasl H, Lee H-S and Marciano W J 2015 Low  $Q^2$  weak mixing angle measurements and rare Higgs decays *Phys. Rev. D* **92** 055005
- [59] Thomas A W, Wang X and Williams A G 2022 Sensitivity of parity-violating electron scattering to a dark photon *Phys. Rev. Lett.* **129** 011807
- [60] Aaltonen T *et al* (CDF collaboration) 2022 High-precision measurement of the W boson mass with the CDF II detector *Science* **376** 170–6
- [61] Thomas A W and Wang X G 2022 Constraints on the dark photon from parity violation and the W mass *Phys. Rev. D* **106** 056017
- [62] Babu K S, Kolda C F and March-Russell J 1996 Leptophobic U(1)  $s$  and the  $R(b)$ – $R(c)$  crisis *Phys. Rev. D* **46** 35–47
- [63] Zheng X, Erler J, Liu Q and Spiesberger H 2021 Accessing weak neutral-current coupling  $g_{AA}^{eq}$  using positron and electron beams at Jefferson Lab *Eur. Phys. J. A* **57** 173
- [64] Erler J, Horowitz C J, Mantry S and Souder P A 2014 Weak polarized electron scattering *Ann. Rev. Nucl. Part. Sci.* **64** 269–98
- [65] Boughezal R, Petriello F and Wiegand D 2021 Disentangling standard model EFT operators with future low-energy parity-violating electron scattering experiments *Phys. Rev. D* **104** 016005
- [66] Charchula K, Schuler G A and Spiesberger H 1994 Combined QED and QCD radiative effects in deep inelastic lepton – proton scattering: the Monte Carlo generator DJANGO6 *Comput. Phys. Commun.* **81** 381–402
- [67] Rodionov E N, Thomas A W and Londergan J T 1994 Charge asymmetry of parton distributions *Mod. Phys. Lett. A* **9** 1799–806
- [68] Mantry S, Ramsey-Musolf M J and Sacco G F 2010 Examination of higher-order twist contributions in parity-violating deep-inelastic electron–deuteron scattering *Phys. Rev. C* **82** 065205
- [69] Zeller G *et al* (NuTeV Collaboration) 2002 A precise determination of electroweak parameters in neutrino nucleon scattering *Phys. Rev. Lett.* **88** 091802
- [70] Londergan J and Thomas A W 2003 Charge symmetry violation corrections to determination of the Weinberg angle in neutrino reactions *Phys. Rev. D* **67** 111901
- [71] Londergan J, Peng J and Thomas A 2010 Charge symmetry at the partonic level *Rev. Mod. Phys.* **82** 2009–52
- [72] Gettratos G G *et al* 2010 Measurement of the  $F_2^n/F_2^p$ ,  $d/u$  ratios and  $A = 3$  EMC effect in deep inelastic electron scattering off the Tritium and Helium mirror nuclei (MARATHON) Jefferson Lab Experiment E12-10-103

- [73] Kuhn S *et al* The structure of the free neutron at large x-Bjorken Jefferson Lab Experiment E12-06-113, 2006 with ? update
- [74] Accardi A, Brady L T, Melnitchouk W, Owens J F and Sato N 2016 Constraints on large-x parton distributions from new weak boson production and deep-inelastic scattering data *Phys. Rev. D* **93** 114017
- [75] Abrams D *et al* (Jefferson Lab Hall A Tritium collaboration) 2022 Measurement of the nucleon  $F_2^n/F_2^p$  structure function ratio by the Jefferson Lab MARATHON Tritium/Helium-3 deep inelastic scattering experiment *Phys. Rev. Lett.* **128** 132003
- [76] Cocuzza C *et al* (Jefferson Lab Angular Momentum (JAM) collaboration) 2021 Isovector EMC effect from global QCD analysis with MARATHON data *Phys. Rev. Lett.* **127** 242001
- [77] Cui Z-F, Gao F, Binosi D, Chang L, Roberts C D and Schmidt S M 2022 Valence quark ratio in the proton *Chin. Phys. Lett.* **39** 041401
- [78] Miller G A and Smith J R 2002 Return of the EMC effect *Phys. Rev. C* **65** 015211
- [79] Smith J R and Miller G A 2002 Return of the EMC effect: finite nuclei *Phys. Rev. C* **65** 055206
- [80] Cloet I, Bentz W and Thomas A 2012 Parity-violating DIS and the flavour dependence of the EMC effect *Phys. Rev. Lett.* **109** 182301
- [81] Schienbein I *et al* 2009 PDF nuclear corrections for charged and neutral current processes *Phys. Rev. D* **80** 094004
- [82] Kovarik K *et al* 2011 Nuclear corrections in neutrino-nucleus DIS and their compatibility with global NPDF analyses *Phys. Rev. Lett.* **106** 122301
- [83] Arrington J 2016 Short-range correlations and their implications for isospin-dependent modification of nuclear quark distributions *EPJ Web Conf.* **113** 01011
- [84] Weinstein L B, Pisetzky E, Higinbotham D W, Gomez J, Hen O and Shneor R 2011 Short range correlations and the EMC effect *Phys. Rev. Lett.* **106** 052301
- [85] Arrington J, Daniel A, Day D, Fomin N, Gaskell D and Solvignon P 2012 A detailed study of the nuclear dependence of the EMC effect and short-range correlations *Phys. Rev. C* **86** 065204
- [86] Shifman M A, Vainshtein A I and Zakharov V I 1979 QCD and resonance physics. Theoretical foundations *Nucl. Phys. B* **147** 385–447
- [87] Shifman M A, Vainshtein A I and Zakharov V I 1979 QCD and resonance physics: applications *Nucl. Phys. B* **147** 448–518
- [88] Shifman M A, Vainshtein A I and Zakharov V I 1978 Remarks on Higgs boson interactions with nucleons *Phys. Lett.* **78B** 443–6
- [89] Durr S *et al* 2008 *Ab initio* determination of light hadron masses *Science* **322** 1224–7
- [90] Borsanyi S *et al* 2015 *Ab initio* calculation of the neutron–proton mass difference *Science* **347** 1452–5
- [91] Ali A *et al* (GlueX collaboration) 2019 First measurement of near-threshold  $J/\psi$  exclusive photoproduction off the proton *Phys. Rev. Lett.* **123** 072001
- [92] Duran B *et al* When color meets gravity; near-threshold exclusive  $J/\psi$  photoproduction on the proton arXiv:2207.05212
- [93] Aaij R *et al* (LHCb collaboration) 2015 Observation of  $J/\psi p$  resonances consistent with pentaquark states in  $\Lambda_b^0 \rightarrow J/\psi K^- p$  decays *Phys. Rev. Lett.* **115** 072001
- [94] Aaij R *et al* (LHCb collaboration) 2019 Observation of a narrow pentaquark state,  $P_c(4312)^+$ , and of two-peak structure of the  $P_c(4450)^+$  *Phys. Rev. Lett.* **122** 222001
- [95] Kharzeev D E 2021 Mass radius of the proton *Phys. Rev. D* **104** 054015
- [96] Hatta Y and Yang D-L 2018 Holographic  $J/\psi$  production near threshold and the proton mass problem *Phys. Rev. D* **98** 074003
- [97] Hatta Y, Rajan A and Yang D-L 2019 Near threshold  $J/\psi$  and  $\Upsilon$  photoproduction at JLab and RHIC *Phys. Rev. D* **100** 014032
- [98] Mamo K A and Zahed I  $J/\psi$  near threshold in holographic QCD: A and D gravitational form factors arXiv:2204.08857
- [99] Mamo K A and Zahed I 2020 Diffractive photoproduction of  $J/\psi$  and  $\Upsilon$  using holographic QCD: gravitational form factors and GPD of gluons in the proton *Phys. Rev. D* **101** 086003
- [100] Guo Y, Ji X-D and Liu Y 2021 QCD analysis of near-threshold photon-proton production of heavy quarkonium *Phys. Rev. D* **103** 096010
- [101] Sun P, Tong X-B and Yuan F 2021 Perturbative QCD analysis of near threshold heavy quarkonium photoproduction at large momentum transfer *Phys. Lett. B* **822** 136655
- [102] Pefkou D A, Hackett D C and Shanahan P E 2022 Gluon gravitational structure of hadrons of different spin *Phys. Rev. D* **105** 054509

- [103] Shanahan P E and Detmold W 2019 Gluon gravitational form factors of the nucleon and the pion from lattice QCD *Phys. Rev. D* **99** 014511
- [104] Baym G *et al* 2018 An assessment of U.S.-based electron-ion collider science Available at: <https://www.nap.edu/read/25171>
- [105] Diehl M 2003 Generalized parton distributions *Phys. Rep.* **388** 41–277
- [106] Belitsky A V and Radyushkin A V 2005 Unraveling hadron structure with generalized parton distributions *Phys. Rep.* **418** 1–387
- [107] Guidal M, Moutarde H and Vanderhaeghen M 2013 Generalized parton distributions in the valence region from deeply virtual Compton scattering *Rep. Prog. Phys.* **76** 066202
- [108] Ji X-D 1997 Gauge-invariant decomposition of nucleon spin *Phys. Rev. Lett.* **78** 610–3
- [109] Goetze K, Polyakov M V and Vanderhaeghen M 2001 Hard exclusive reactions and the structure of hadrons *Prog. Part. Nucl. Phys.* **47** 401–515
- [110] Čuić M, Kumerički K and Schäfer A 2020 Separation of quark flavors using deeply virtual Compton scattering data *Phys. Rev. Lett.* **125** 232005
- [111] Frankfurt L L, Pobylitsa P V, Polyakov M V and Strikman M 1999 Hard exclusive pseudoscalar meson electroproduction and spin structure of a nucleon *Phys. Rev. D* **60** 014010
- [112] Diehl M and Sapeta S 2005 On the analysis of lepton scattering on longitudinally or transversely polarized protons *Eur. Phys. J. C* **41** 515–33
- [113] Belitsky A V 2004 Renormalons in exclusive meson electroproduction *AIP Conf. Proc.* (<https://doi.org/10.1063/1.1664310>)
- [114] Airapetian A *et al* (HERMES collaboration) 2010 Single-spin azimuthal asymmetry in exclusive electroproduction of  $\pi^+$  mesons on transversely polarized protons *Phys. Lett. B* **682** 345–50
- [115] Goloskokov S V and Kroll P 2010 An attempt to understand exclusive  $\pi^+$  electroproduction *Eur. Phys. J. C* **65** 137–51
- [116] Ji X-D 1997 Deeply virtual Compton scattering *Phys. Rev. D* **55** 7114–25
- [117] Belitsky A V, Mueller D and Kirchner A 2002 Theory of deeply virtual Compton scattering on the nucleon *Nucl. Phys. B* **629** 323–92
- [118] Jefferson Lab Hall A *et al* 2006 Scaling tests of the cross-section for deeply virtual Compton scattering *Phys. Rev. Lett.* **97** 262002
- [119] Defurne M *et al* (Jefferson Lab Hall A collaboration) 2015 E00-110 experiment at Jefferson Lab Hall A: deeply virtual Compton scattering off the proton at 6 GeV *Phys. Rev. C* **92** 055202
- [120] Girod F X *et al* (CLAS collaboration) 2008 Measurement of deeply virtual Compton scattering beam-spin asymmetries *Phys. Rev. Lett.* **100** 162002
- [121] Jo H S *et al* (CLAS collaboration) 2015 Cross sections for the exclusive photon electroproduction on the proton and generalized parton distributions *Phys. Rev. Lett.* **115** 212003
- [122] Airapetian A *et al* (HERMES collaboration) 2001 Measurement of the beam spin azimuthal asymmetry associated with deeply virtual Compton scattering *Phys. Rev. Lett.* **87** 182001
- [123] Airapetian A *et al* (HERMES collaboration) 2012 Beam-helicity and beam-charge asymmetries associated with deeply virtual Compton scattering on the unpolarised proton *J. High Energy Phys.* **JHEP07(2012)032**
- [124] Airapetian A *et al* (HERMES collaboration) 2010 Exclusive lepton production of real photons on a longitudinally polarised hydrogen target *J. High Energy Phys.* **JHEP06(2010)019**
- [125] Airapetian A *et al* (HERMES collaboration) 2008 Measurement of azimuthal asymmetries with respect to both beam charge and transverse target polarization in exclusive electroproduction of real photons *J. High Energy Phys.* **JHEP06(2008)066**
- [126] Airapetian A *et al* (HERMES collaboration) 2011 Measurement of double-spin asymmetries associated with deeply virtual Compton scattering on a transversely polarized hydrogen target *Phys. Lett. B* **704** 15–23
- [127] Airapetian A *et al* (HERMES collaboration) 2007 The beam-charge Azimuthal asymmetry and deeply virtual Compton scattering *Phys. Rev. D* **75** 011103
- [128] Airapetian A *et al* (HERMES collaboration) 2009 Separation of contributions from deeply virtual Compton scattering and its interference with the Bethe–Heitler process in measurements on a hydrogen target *J. High Energy Phys.* **JHEP11(2009)083**
- [129] Airapetian A *et al* (HERMES collaboration) 2010 Nuclear-mass dependence of azimuthal beam-helicity and beam-charge asymmetries in deeply virtual Compton scattering *Phys. Rev. C* **81** 035202
- [130] Camsonne A *et al* 2006 Measurements of electron-helicity dependent cross sections of deeply virtual Compton scattering with CEBAF at 12 GeV Jefferson Lab Experiment E12-06-114



- [131] Biselli A *et al* 2006 Deeply virtual Compton scattering with CLAS12 at 11 GeV Jefferson Lab Experiment E12-06-119
- [132] Mazouz M *et al* (Jefferson Lab Hall A collaboration) 2007 Deeply virtual compton scattering off the neutron *Phys. Rev. Lett.* **99** 242501
- [133] Niccolai S *et al* 2011 Deeply virtual Compton scattering on the neutron with CLAS12 at 11 GeV Jefferson Lab Experiment E12-11-003
- [134] Chatagnon P *et al* (CLAS Collaboration) 2021 First measurement of timelike Compton scattering *Phys. Rev. Lett.* **127** 262501
- [135] Burkardt M 2000 Impact parameter dependent parton distributions and off- forward parton distributions for  $\zeta^0$  *Phys. Rev. D* **62** 071503
- [136] Guidal M and Vanderhaeghen M 2003 Double deeply virtual compton scattering off the nucleon *Phys. Rev. Lett.* **90** 012001
- [137] Belitsky A-V and Müller D 2003 Exclusive electroproduction of lepton pairs as a probe of nucleon structure *Phys. Rev. Lett.* **90** 022001
- [138] Anikin I-V *et al* 2018 Nucleon and nuclear structure through dilepton production *Acta Phys. Polon. B* **49** 741–84
- [139] Zhao S *et al* 2021 Double deeply virtual Compton scattering with positron beams at SoLID *Eur. Phys. J. A* **57** 240
- [140] Boer M *et al* 2015 Measurement of double deeply virtual compton scattering in the di-muon channel with the SoLID spectrometer Jefferson Lab Letter-of-Intent LO12-15-005
- [141] Zhao S 2020 Studying the nucleon structure via double deeply virtual compton scattering at the Jefferson laboratory *PhD Thesis* Université Paris Saclay, Orsay, France
- [142] Wandzura S and Wilczek F 1977 Sum rules for spin dependent electroproduction: test of relativistic constituent quarks *Phys. Lett. B* **72** 195–8
- [143] Adeva B *et al* (Spin Muon collaboration) 1998 Spin asymmetries A(1) and structure functions g1 of the proton and the deuteron from polarized high-energy muon scattering *Phys. Rev. D* **58** 112001
- [144] Abe K *et al* (E143 collaboration) 1998 Measurements of the proton and deuteron spin structure functions g(1) and g(2) *Phys. Rev. D* **58** 112003
- [145] Wilson K G 1969 Nonlagrangian models of current algebra *Phys. Rev.* **179** 1499–512
- [146] Armstrong W R *et al* 2020 A precision measurement of inclusive  $g_2^n$  and  $d_2^n$  with SoLID on a polarized  $^3\text{He}$  target at 8.8 and 11 GeV Jefferson Lab RunGroup Experiment E12-11-007A/E12-10-006E
- [147] Airapetian A *et al* (HERMES collaboration) 2010 Effects of transversity in deep-inelastic scattering by polarized protons *Phys. Lett. B* **693** 11–6
- [148] Adolph C *et al* (COMPASS collaboration) 2015 Collins and Sivers asymmetries in muonproduction of pions and kaons off transversely polarised protons *Phys. Lett. B* **744** 250–9
- [149] Zhao Y X *et al* (Jefferson Lab Hall A collaboration) 2014 Single spin asymmetries in charged kaon production from semi-inclusive deep inelastic scattering on a transversely polarized  $^3\text{He}$  target *Phys. Rev. C* **90** 055201
- [150] Chiu M *et al* 2015 RD proposal for (Sub) 10 picosecond timing detectors at the EIC *eRD10 Progress Report*
- [151] Wang Y *et al* 2013 A MRPC prototype for SOLID-TOF in JLab *JINST* **8** P03003
- [152] Pisano S and Radici M 2016 Di-hadron fragmentation and mapping of the nucleon structure *Eur. Phys. J. A* **52** 155
- [153] Luo X, Sun H, Li J, Xie Y-L and Tichouk 2019 Double spin asymmetry in dihadron production in SIDIS off a longitudinally polarized nucleon target *Phys. Rev. D* **100** 094036
- [154] Radici M and Bacchetta A 2018 First extraction of transversity from a global analysis of electron–proton and proton–proton data *Phys. Rev. Lett.* **120** 192001
- [155] Mirazita M *et al* (CLAS collaboration) 2021 Beam spin asymmetry in semi-inclusive electroproduction of hadron pairs *Phys. Rev. Lett.* **126** 062002
- [156] Courtoy A, Miramontes A S, Avakian H, Mirazita M and Pisano S 2022 Extraction of the higher-twist parton distribution e(x) from CLAS data *Phys. Rev. D* **106** 014027
- [157] Dilks C (CLAS collaboration) 2022 Multidimensional partial wave analysis of SIDIS dihadron beam spin asymmetries at CLAS12 *SciPost Phys. Proc.* **8** 152
- [158] Puckett A J R *et al* 2012 Final analysis of proton form factor ratio data at  $Q^2 = 4.0, 4.8$  and  $5.6 \text{ GeV}^2$  *Phys. Rev. C* **85** 045203

- [159] Christy M E *et al* 2022 Form factors and two-photon exchange in high-energy elastic electron–proton scattering *Phys. Rev. Lett.* **128** 102002
- [160] Rachek I A *et al* 2015 Measurement of the two-photon exchange contribution to the elastic  $e^+p$  scattering cross sections at the VEPP-3 storage ring *Phys. Rev. Lett.* **114** 062005
- [161] Rimal D *et al* (CLAS collaboration) 2017 Measurement of two-photon exchange effect by comparing elastic  $e^+p$  cross sections *Phys. Rev. C* **95** 065201
- [162] Henderson B S *et al* (OLYMPUS collaboration) 2017 Hard two-photon contribution to elastic lepton-proton scattering: determined by the OLYMPUS experiment *Phys. Rev. Lett.* **118** 092501
- [163] Accardi A *et al* 2021 An experimental program with high duty-cycle polarized and unpolarized positron beams at Jefferson Lab *Eur. Phys. J. A* **57** 261
- [164] Christ N and Lee T D 1966 Possible tests of Cst and Tst invariances in  $l^\pm + N \rightarrow l^\pm + \Gamma$  and  $A \rightarrow B + e^+ + e^-$  *Phys. Rev.* **143** 1310–21
- [165] Metz A, Schlegel M and Goeke K 2006 Transverse single spin asymmetries in inclusive deep-inelastic scattering *Phys. Lett. B* **643** 319
- [166] Metz A, Pitonyak D, Schäfer A, Schlegel M, Vogelsang W and Zhou J 2012 Single-spin asymmetries in inclusive deep inelastic scattering and multiparton correlations in the nucleon *Phys. Rev. D* **86** 094039
- [167] Schlegel M 2013 Partonic description of the transverse target single-spin asymmetry in inclusive deep-inelastic scattering *Phys. Rev. D* **87** 034006
- [168] Airapetian A *et al* (HERMES collaboration) 2010 Search for a two-photon exchange contribution to inclusive deep-inelastic scattering *Phys. Lett. B* **682** 351–4
- [169] Katich J *et al* 2014 Measurement of the target-normal single-spin asymmetry in deep-inelastic scattering from the reaction  $^3\text{He}^\uparrow(e, e')X$  *Phys. Rev. Lett.* **113** 022502
- [170] Zhang Y W *et al* 2015 Measurement of the target-normal single-spin asymmetry in quasielastic scattering from the reaction  $^3\text{He}^\uparrow(e, e')$  *Phys. Rev. Lett.* **115** 172502
- [171] Afanasev A, Strikman M and Weiss C 2008 Transverse target spin asymmetry in inclusive DIS with two-photon exchange *Phys. Rev. D* **77** 014028
- [172] Averett A *et al* 2014 Target single spin asymmetry measurements in the inclusive deep-inelastic reaction on transversely polarized proton and neutron ( $^3\text{He}$ ) targets using the SoLID spectrometer Jefferson Lab Run group Experiment E12-11-108A/E12-10-006A
- [173] Androić D *et al* (QWeak collaboration) 2021 Measurement of the beam-normal single-spin asymmetry for elastic electron scattering from  $^{12}\text{C}$  and  $^{27}\text{Al}$  *Phys. Rev. C* **104** 014606
- [174] Adhikari D *et al* (PREX, CREX collaboration) 2022 New measurements of the beam-normal single spin asymmetry in elastic electron scattering over a range of Spin-0 nuclei *Phys. Rev. Lett.* **128** 142501
- [175] Deur A, Brodsky S J and De Téramond G F The spin structure of the nucleon arXiv:1807.05250
- [176] Cates G *et al* 2016 First measurement of the  $e^-^3\text{He}$  parity violating deep inelastic scattering asymmetry using an upgraded polarized  $^3\text{He}$  target Jefferson Lab Letter of Intent LOI12-16-007
- [177] Kubota Y *et al* (CLEO collaboration) 1992 The CLEO-II detector *Nucl. Instrum. Meth. A* **320** 66–113
- [178] Coffman D M, Ehrlich R D, Gray S W, Nordberg M E and Pisharody M 1990 The CLEO-II detector magnet: design, tests, and performance *IEEE Trans. Nucl. Sci.* **37** 1172–5
- [179] Sauli F 1997 GEM: a new concept for electron amplification in gas detectors *Nucl. Instrum. Meth. A* **386** 531–4
- [180] Ketzer B, Weitzel Q, Paul S, Sauli F and Ropelewski L 2004 Performance of triple GEM tracking detectors in the COMPASS experiment *Nucl. Instrum. Meth. A* **535** 314–8
- [181] Xiong W *et al* 2019 A small proton charge radius from an electron–proton scattering experiment *Nature* **575** 147–50
- [182] Atoian G S *et al* 2008 An improved Shashlyk calorimeter *Nucl. Instrum. Meth. A* **584** 291–303
- [183] Sulkosky V *et al* 2016 Studies of relative gain and timing response of fine-mesh photomultiplier tubes in high magnetic fields *Nucl. Instrum. Meth. A* **827** 137–44
- [184] Wang Y *et al* 2009 A prototype of a high rating MRPC *Chin. Phys. C* **33** 374–7
- [185] Wang J *et al* 2012 A realistic design of the CBM-TOF wall based on modules commissioned in-beam *J. Instrum.* **7** P10004
- [186] Lyu P *et al* 2018 Performance study of a real-size mosaic high-rate MRPC *J. Instrum.* **13** P06016
- [187] Yu Y *et al* (CMS RPC collaboration) 2019 R&D of a real-size mosaic MRPC within the framework of the CMS muon upgrade *J. Instrum.* **14** C10042



- [188] SOLID\_GEMC, GitHub repository. [https://github.com/JeffersonLab/solid\\_gemc](https://github.com/JeffersonLab/solid_gemc), started 2010.
- [189] GEMC, GEant4 Monte-Carlo. <https://gemc.jlab.org>, started 2007.
- [190] Allison J *et al* 2016 Recent developments in Geant4 *Nucl. Instrum. Meth. A* **835** 186–225
- [191] libsolgem, GitHub repository. <https://github.com/xweizhi/libsolgem>, started 2011
- [192] SoLIDTracking, GitHub repository. <https://github.com/xweizhi/SoLIDTracking>, started 2016
- [193] Xiong W 2017 SoLID GEM digitization and tracking Technical Note, SoLID Document 96-v1
- [194] Peng C *et al* 2022 Performance of photosensors in a high-rate environment for gas Cherenkov detectors *J. Instrum.* **17** P08022
- [195] Natarajan C M, Tanner M G and Hadfield R H 2012 Superconducting nanowire single-photon detectors: physics and applications *Supercond. Sci. Technol.* **25** 063001
- [196] Anderson R L and Muons Excess 1976 Excess Muons and new results in psi photoproduction *Int. Conf. on the Production of Particles with New Quantum Numbers 4* <http://slac.stanford.edu/pubs/slacpubs/1500/slac-pub-1741.pdf>
- [197] Gittelman B, Hanson K M, Larson D, Loh E, Silverman A and Theodosiou G 1975 Photoproduction of the psi (3100) Meson at 11 GeV *Phys. Rev. Lett.* **35** 1616
- [198] Zheng X *et al* 2021 Measurement of the asymmetry  $A_d^{e^+e^-}$  between  $e^+-^2\text{H}$  and  $e^--^2\text{H}$  deep inelastic scattering using SoLID and PEPPo at JLab Jefferson Lab Proposal PR12-21-006
- [199] Argento A *et al* 1983 Electroweak asymmetry in deep inelastic muon–nucleon scattering *Phys. Lett. B* **120** 245